学位論文

# Study on electroweak parameters by measurement of the total hadronic cross section in $e^+e^-$ annihilation

(電子・陽電子対消滅におけるハドロン生成全断面積の測定による電弱理論パラメータに関する研究)

１９９４年

宮林謙吉

(1)

# Study on electroweak parameters by measurement of the total hadronic cross section in $e^+e^-$ annihilation

KENKICHI MIYABAYASHI

*Department of Physics, Nagoya University**
*Nagoya 464, Japan*

December 1994

Ph.D Dissertation

---

**Present address : Department of physics, Nara Women's University, Nara, 630, Japan*

## Abstract

The total hadronic cross section in $e^+e^-$ annihilation was measured with the TOPAZ detector at TRISTAN. A total of 9146 hadronic events was selected from the data corresponding to 90.8pb$^{-1}$ at $\sqrt{s}$=57.77GeV. In this measurement, to make the resultant value model-independent, only the QED corrections up to $O(\alpha^2)$ + exponentiation was applied. As the result,

$$\sigma_h = 143.6 \pm 1.5(\text{stat.}) \pm 4.5(\text{syst.})\text{pb}.$$

was obtained.

From this measurement, the effective form factor of $\gamma\gamma$ propagator was determined to be

$$1/\bar{\alpha}(57.77^2 GeV^2) = 128.6^{+0.9}_{-0.8}(\text{stat})^{+2.7}_{-2.5}(\text{sys})$$

This result is the first direct measurement of $\bar{\alpha}(q^2)$ at high energy and is the first clear evidence of $SU(2)\times U(1)$ propagators running.

By combining with LEP data, our data give a constraint to the size of $\gamma - Z$ interference. The coefficient of the interference is found to be $J_{had}$=0.10$\pm$0.26. The mass of $Z^0$ boson in S-matrix approach was also obtained to be $\bar{M}_Z$=91.151$\pm$0.008 GeV from a model-independent four parameters fit.

# Contents

# List of Figures



# List of Tables

# 1 Introduction

It is known that there are four fundamental forces in the universe; gravitational, weak, electromagnetic and strong interactions. In the particle physics at the energy scale of 100GeV, the gravity between the particles is not important effect because it is $10^{-40}$ times weaker than the other interactions. The Standard Model (SM) has been succeeding to describe the structure of fermion multiplets and the remained three interactions with gauge bosons. It is $SU(2)_L \times U(1)_Y \times SU(3)_C$ gauge group theory, where $SU(2)_L \times U(1)_Y$ corresponds to the electroweak interactions formulated by Glashow-Salam-Weinberg, and the $SU(3)_C$ denote the strong interaction described by the quantum chromodynamics (QCD). Though this model successfully explained all the available experimental data, it should be regarded as an "effective theory" at the currently available energy scale, because there are many free parameters in this model.

The electroweak precision measurements have been established the validity of SM and arrived at the new stage where we can test not only the SM but also search the new physics beyond the SM. For instance, it was reported that recent precise electroweak measurements support the supersymmetric $SU(5)$ Grand Unified Theory which enable the unification of the three coupling constants at around $10^{16}$GeV.

The total hadronic cross section is one of the fundamental observables to test the SM or such the possible new pictures. In order to extract physics results from $e^+e^-$ annihilation process, it is inevitable to make a radiative correction. In the previous analyses at PEP, PETRA and TRISTAN, the Born ("tree level") cross section was obtained by so called "full electroweak correction". However, since we must assume the SM loop corrections and correct them to get the Born cross section, the obtained results strongly depend on the SM and its unknown parameters such as masses of the top quark and the Higgs boson.

In this thesis, we present the total hadronic cross section with only the QED correction, and from this data, two model-independent analyses; determination of QED effective form factor $\bar{\alpha}(q^2)$ which is the $\gamma\gamma$ propagator and

determination of $\gamma$-$Z$ interference are performed.

The organization of this thesis is as follows; Chapter 2 reviews the Standard Model and treatment of radiative corrections. The cross section formulae with the effective form factors and S-matrix approach are summarized there. The experimental apparatus, TRISTAN $e^+e^-$ collider and the TOPAZ detector are briefly reviewed in Chapter 3. Chapter 4 is devoted to quick review of the data processing. Multihadron event selection and derivation of the total hadronic cross section are discussed in Chapter 5. Estimation of systematic errors are also described. Determination of QED effective form factor $\bar{\alpha}(q^2)$ and determination of $\gamma$-$Z$ interference are discussed in Chapter 6. Chapter 7 concludes this thesis.

# 2 Theoretical Framework

In this section, the Standard Model and the formalism for model-independent analyses are briefly reviewed. The former is comprised by the electroweak theory formulated by Glashow-Salam-Weinberg[1] and the quantum chromodynamics(QCD), and the latter is expressed by the treatment of radiative corrections. And then, in the section 2.5, the lineshape fit formalism to determine $Z^0$ parameters are explained.

## 2.1 The electoweak theory

The electroweak theory stands on the $SU(2)_L \times U(1)_Y$ gauge symmetry which requires four gauge bosons. Three of them belong to weak isospin triplet $SU(2)_L$ $(W^i_\mu)$ and the remained one belong to weak hypercharge group $U(1)_Y$ $(B_\mu)$. The suffix "$L$" denotes left-handed because $SU(2)$ transformations only apply to the left handed states, and "$Y$" corresponds to the weak hypercharge which is the generator of $U(1)$ symmetry. The constituent fermions in the electroweak theory are leptons and quarks. They are categorized to three groups called "generation". The left handed fermions form $SU(2)$ doublets but the right handed ones are $SU(2)$ siglets. In the quark sector, there are mixings between the generations. These fermions are expressed as,

$$\Psi_L = \begin{pmatrix} \nu_l \\ l^-_L \end{pmatrix}, \quad \Psi_R = l^-_R \quad \text{for leptons} \tag{1}$$

$$\Psi_L = \begin{pmatrix} u_{iL} \\ d'_{iL} \end{pmatrix}, \quad \begin{array}{l} \Psi_R = u_{iR} \quad \text{for up type quarks, and} \\ \Psi_R = d'_{iR} \quad \text{for down type quarks} \end{array} \tag{2}$$

where $l$=$e, \mu, \tau$, $d'_i = \sum_j V_{ij} d_j$ and $V_{ij}$ is the Kobayashi-Maskawa mixing matrix[2], $i$ and $j$ denote the quarks generation number.

The charged current gauge fields are defined by:

$$W^\pm_\mu = \frac{W^1_\mu \mp W^2_\mu}{\sqrt{2}} \tag{3}$$

The electromagnetic field, $A_\mu$, and the neutral current weak field, $Z_\mu$, are linear combinations of $B_\mu$ and another neutral weak gauge field $W_\mu^3$:

$$\begin{aligned} A_\mu &= B_\mu \cos\theta_W + W_\mu^3 \sin\theta_W \\ Z_\mu &= -B_\mu \sin\theta_W + W_\mu^3 \cos\theta_W \end{aligned} \tag{4}$$

where $\theta_W$ is the weak mixing angle (Weinberg angle) and is defined as the ratio of the two independent gauge coupling constants:

$$\tan\theta_W = \frac{g'}{g} \tag{5}$$

In fact, the weak gauge bosons are massive. If we did not give the special treatment to explain it, unrenormarizable divergences appear because of the mass terms of the gauge bosons. Therefore, Higgs mechanism was introduced and it predicts the Higgs boson as a result of the spontenious symmetry breaking. The masses of the particles are expressed as the strength of the interaction with the Higgs boson. In the minimal model, one Higgs doublet is predicted and more doublets can exist.

## 2.2 Quantum chromodynamics

The strong interaction is described by quantum chromodynamics(QCD) which is non-Abelian $SU(3)_C$ gauge theory, where the suffix"$C$" denotes the "color" carried by quarks and gluons. As a nature of non-Abelian gauge theories, QCD includes gluon self-coupling. The number of quark flavors and the self-coupling nature causes the "asymptotic freedom", i.e. the strong coupling constant of QCD, $\alpha_s$, decreases as momentum transfer increases. This is a remarkable characteristics of QCD. Hence, the high energy $e^+e^- \to hadrons$ reaction allow us QCD purtabative calculation, however, in the low momentum transfer region, $\alpha_s$ becomes so large that purtabative method is not applicable. Because quarks and gluons turn into colorless hadrons in such region, the hadronization process only can be described by the phenomenological models.

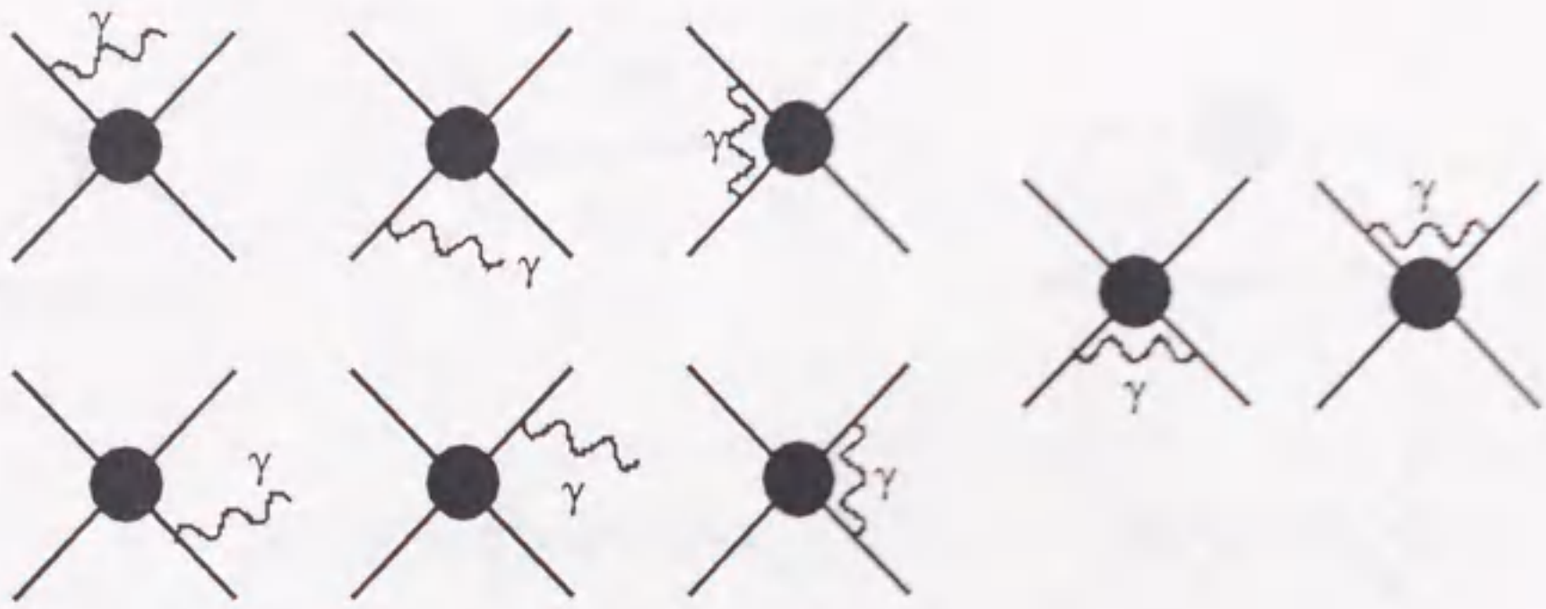

Figure 1: The diagrams appear in $O(\alpha)$ QED corrections.

## 2.3 Radiative correction

The gauge bosons and fermion multiplets of the electroweak theory were explained in the previous subsections. In the real world, photon radiation from initial or final state fermions and the quantum corrections (loop corrections) must be taken into account in order to compare the theory and the experiments. The whole corrections are categorized into two gauge invariant subsets : the QED corrections and the weak corrections[3].

### 2.3.1 The QED corrections

"QED corrections" consist of the corrections by real photon emissions and the loop of virtual photon. The diagrams with these $O(\alpha)$ correction added to the four fermi amplitude are shown in Fig.1. The separation of the QED corrections is sensible due to the following reasons; (i) they form a gauge invariant subset and (ii) they depend on the details of the experiments via the cuts because the emitted photons change the event shape. Therefore their proper treatment is needed to make the physics analysis on a data sample free from detector dependence. On the other hand, since the QED correction depends only the mass and the charge of initial or final state fermions, they are well known except the small uncertainties of the higher order corrections in spite of the existence of some singularities.

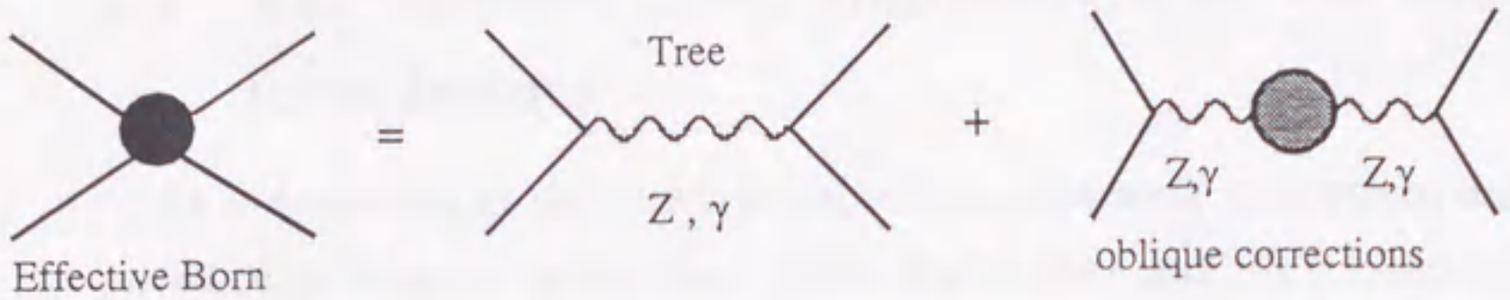


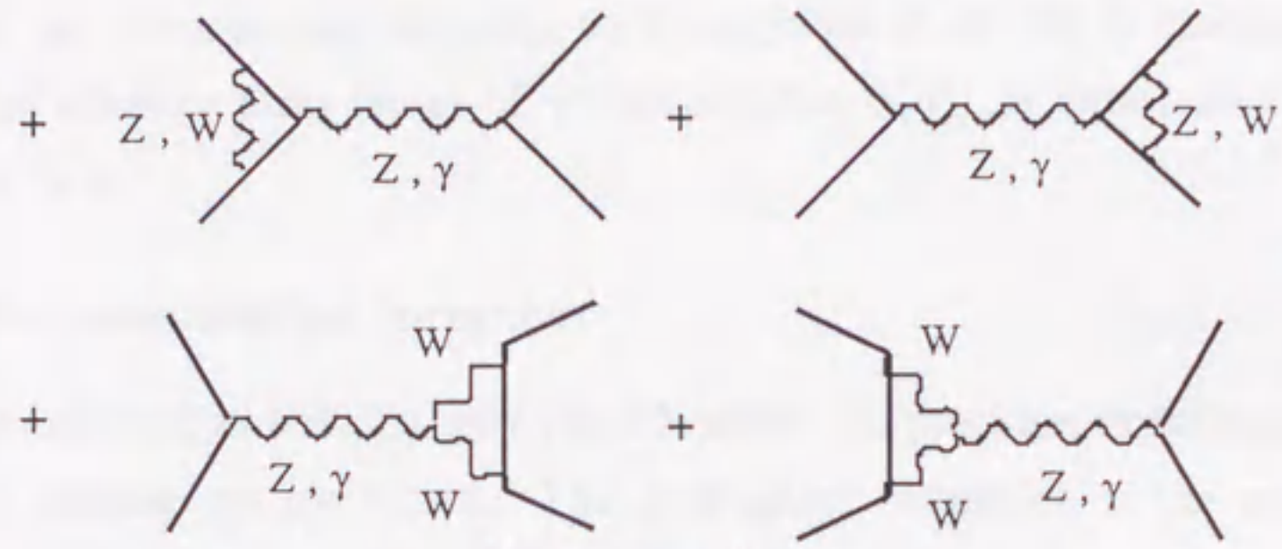


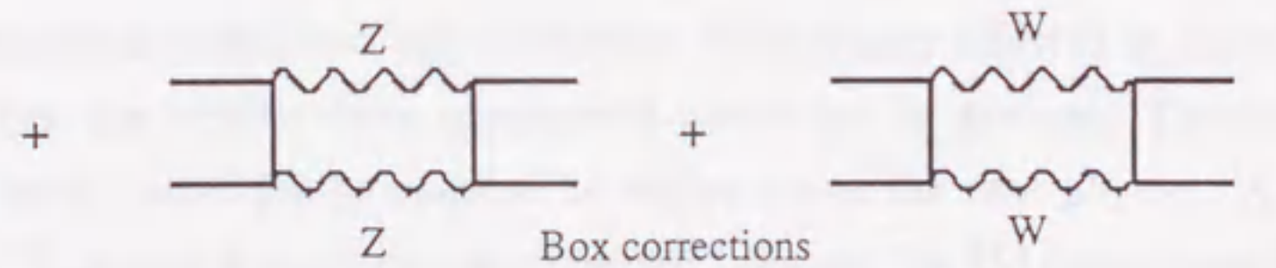


Figure 2: The diagrams appear in $O(\alpha)$ weak corrections.

### 2.3.2 The weak corrections

"Weak corrections" in SM are comprised of one-loop diagrams shown in Fig.2. They are divided into three parts; one is the vacuum polarization of gauge boson which is called oblique[4] correction or propagator[5] correction, the remained two are the vertex corrections and the box corrections with the heavy gauge bosons ($W$ and $Z$). Since these corrections do not change the event shape, they are detector independent. They also include the more subtle part of the electroweak theory beyond the lowest order and the potential "new physics" objects. The four fermi amplitude including the whole weak corrections is called "effective Born" amplitude.

## 2.4 The effective Born amplitude with the effective form factors

As is described in the previous subsection, the weak corrections are comprised by propagator corrections, vertex corrections and box corrections. The calculation of them have been done by the various schemes[7, 8, 9, 10]. In this subsection, the cross section formulae by K.Hagiwara et.al. [10] is discussed because the effective form factor of $\gamma\gamma$ propagator, $\bar{\alpha}(q^2)$, is determined in accordance to it.

### 2.4.1 The cross section formulae

In the framework in Ref.[10], new particle affect the precision experiments mainly via propagator correction. The propagator correction is the most dominant components in the whole weak correction, and it is independent from the external fermion legs of the Feynman diagrams("process independent"). Although vertex and box corrections are actually affected by the new physics, they are smaller than propagator correction in general. Therefore the propagator correction is essential to argue about the new physics. And, $SU(2) \times U(1)$ gauge symmetry are respected because the SM corrections are precisely calculable and a signature of physics beyond the SM can be found as our inability to fit the experimental data.

Hence, as shown in Fig.3, four $q^2$ dependent charge form factors were introduced. They are $\bar{e}^2(q^2)=4\pi\bar{\alpha}(q^2)$, $\bar{g_z}^2(q^2)$, $\bar{s}^2(q^2)$ and $\bar{g_w}^2(q^2)$ corresponding to $\gamma\gamma$, $ZZ$, $\gamma Z$ and $WW$ propagator, respectively. These four form factors at each $q^2$ can be regarded as independent parameters of the electroweak theory . Therefore the measurements of them at various $q^2$ is important to see the new physics beyond the SM. After removal of the QED corrections, the observables in the precision measurements are expressed by the effective Born amplitudes and they can be written down by the S-matrix element responsible to the generic four fermion process[10]:

$$T_{ij} = M_{ij} J_i J_j \tag{6}$$

where $J_i^\mu$ and $J_j^\mu$ denotes currents without coupling factors, that's, $J_i^\mu = \bar{\Psi}_f \gamma^\mu P_\alpha \Psi_f$ for $i=f_\alpha$($f$ is the flavor of the fermion and $\alpha$ is helicity of the

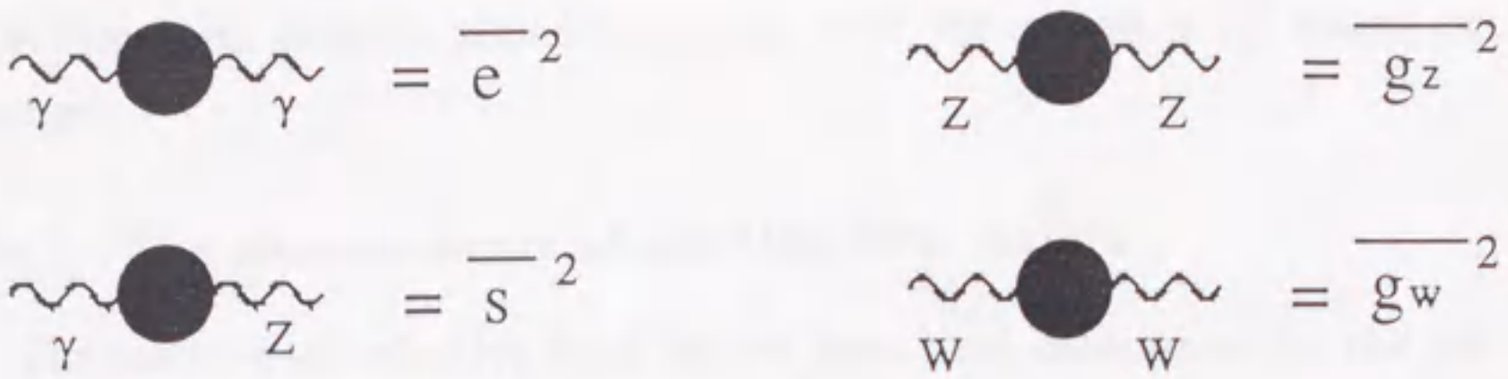


Figure 3: The four effective form factors

fermion current), where $P_L = (1-\gamma^5)/2$ and $P_R = (1+\gamma^5)/2$ are chiral projectors. The effective Born amplitude for neutral current process was found to be:

$$\begin{aligned}
M_{ij}^{NC} &= \frac{Q_i Q_j}{s}[\bar{e}^2(s) + \hat{e}^2(\Gamma_1^i + \Gamma_1^j)(s) - i\hat{e}^2\Delta_{\gamma\gamma}(s)] \\
&+ \hat{e}^2[(Q_i I_{3j}\frac{\bar{\Gamma}_2^j(s)}{s} + I_{3i}Q_j\frac{\bar{\Gamma}_2^i(s)}{s}] \\
&+ \frac{1}{s - M_Z^2 + is(\Gamma_Z/M_Z)} \\
&\times \{(I_{3i} - Q_i\hat{s}^2)(I_{3j} - Q_j\hat{s}^2)[\bar{g_z}^2(s) + \hat{g_Z}^2(\Gamma_1^i + \Gamma_1^j)(s) - i\hat{g_Z}^2\Delta_{ZZ}(s)] \\
&+ (I_{3i} - Q_i\hat{s}^2)\hat{g_Z}^2[I_{3j}(\hat{c}^2\bar{\Gamma}_2^j + \Gamma_3^j)(s) + \Gamma_4^j(s) - Q_j(\bar{s}^2(s) - \hat{s}^2 + i\Delta_{\gamma Z}(s))] \\
&+ (I_{3j} - Q_j\hat{s}^2)\hat{g_Z}^2[I_{3i}(\hat{c}^2\bar{\Gamma}_2^i + \Gamma_3^i)(s) + \Gamma_4^i(s) - Q_i(\bar{s}^2(s) - \hat{s}^2 + i\Delta_{\gamma Z}(s))]\} \\
&+ B_{ij}^{NC}(s,t) \qquad (7)
\end{aligned}$$

In this formula, the three of the four effective form factors, $\bar{e}^2$, $\bar{g}_z^2$ and $\bar{s}^2$ are recognized and the hatted couplings $\hat{e}$=$\hat{g}\hat{s}$=$\hat{g}_z\hat{s}\hat{c}$ are renormarized in the modified minimal subtraction scheme($\overline{\rm MS}$ scheme). $\Delta_{\gamma\gamma}$, $\Delta_{\gamma Z}$ and $\Delta_{ZZ}$ denote imaginary parts of the propagator correction factors. $\Gamma_n^{fa}(s)$ and $B_{ij}$ are the vertex functions and the box functions, respectively.

Therefore, using these charge form factors, we can write this amplitude in a simplified form;

$$\begin{aligned}
\frac{Q_i Q_j}{s}4\pi\bar{\alpha}(s) &+ \frac{\bar{g_z}^2(s)}{s - M_Z{}^2 + is(\Gamma_Z/M_Z)}[I_{3i} - Q_i\bar{s}^2(s)][I_{3j} - Q_j\bar{s}^2(s)] \\
&+ \text{Vertex corrections} \\
&+ \text{Box corrections} \qquad (8)
\end{aligned}$$

The first term denotes photon exchange, and the second is $Z^0$ boson exchange.

### 2.4.2 The measurements of effective form factors

The electroweak effective form factors have been determined by the low energy experiments and LEP/SLC experiments. The fine structure constant $\alpha=\bar{\alpha}(0)$ is measured with extreme precision. And the weak couplings $\bar{g_z}^2(0)$, $\bar{s}^2(0)$ and $\bar{g_w}^2(0)$ are actually measured by the low energy experiments. LEP experiments have measured $\bar{g_z}^2({M_Z}^2)$ and $\bar{s}^2({M_Z}^2)$ very precisely by $Z^0$ line-shape analyses and the forward-backward asymmetry measurements. And, since the running of $\bar{g_z}^2(q^2)$ and $\bar{s}^2(q^2)$ are small, their running are not so significant. These are shown in Fig.4(b)(c).

On the contrary, the running of $\gamma\gamma$ effective form factor, $\bar{\alpha}(q^2)$ is expected to be significantly observed (Fig.4(a)). But because LEP/SLC experiments have no sensitivity to determine $\bar{\alpha}({M_Z}^2)$, they believe in $\bar{\alpha}({M_Z}^2)$ calculated by the Standard Model. Of course $\bar{g_z}^2({M_Z}^2)$ and $\bar{s}^2({M_Z}^2)$ can be translated into $\bar{\alpha}({M_Z}^2)$ according to the SM, but it is not meaningful from the point of view described in the previous subsubsection.

At TRISTAN, $\bar{\alpha}(q^2)$ and $\bar{g_z}^2(q^2)$ can be determined by the total cross section and forward-backward asymmetry of the fermion pair production. Hence TRISTAN is a highest energy point for direct observation of $\bar{\alpha}(q^2)(=\bar{e}^2(q^2)/4\pi)$.

### 2.4.3 New interactions in the electroweak bosonic sector

The signature of the new physics appears as 6-dimensional operators(The higher dimensional ones are expected to be small). It was pointed out and generally formulated by B.Grinstein and M.B.Wise [11]. Historical example was the weak four-fermi interaction. Therefore, the lagrangian $\mathcal{L}$ can be written in the following formula,

$$\mathcal{L} = \mathcal{L}_{SM} + \sum_i \frac{f_i^{(6)}}{\Lambda^2} O_i^{(6)} \tag{9}$$

where $\Lambda$, $O_i^{(6)}$ and $f_i^{(6)}$ denote the mass scale of the new physics, 6-dimensional operator and its coefficient, respectively.

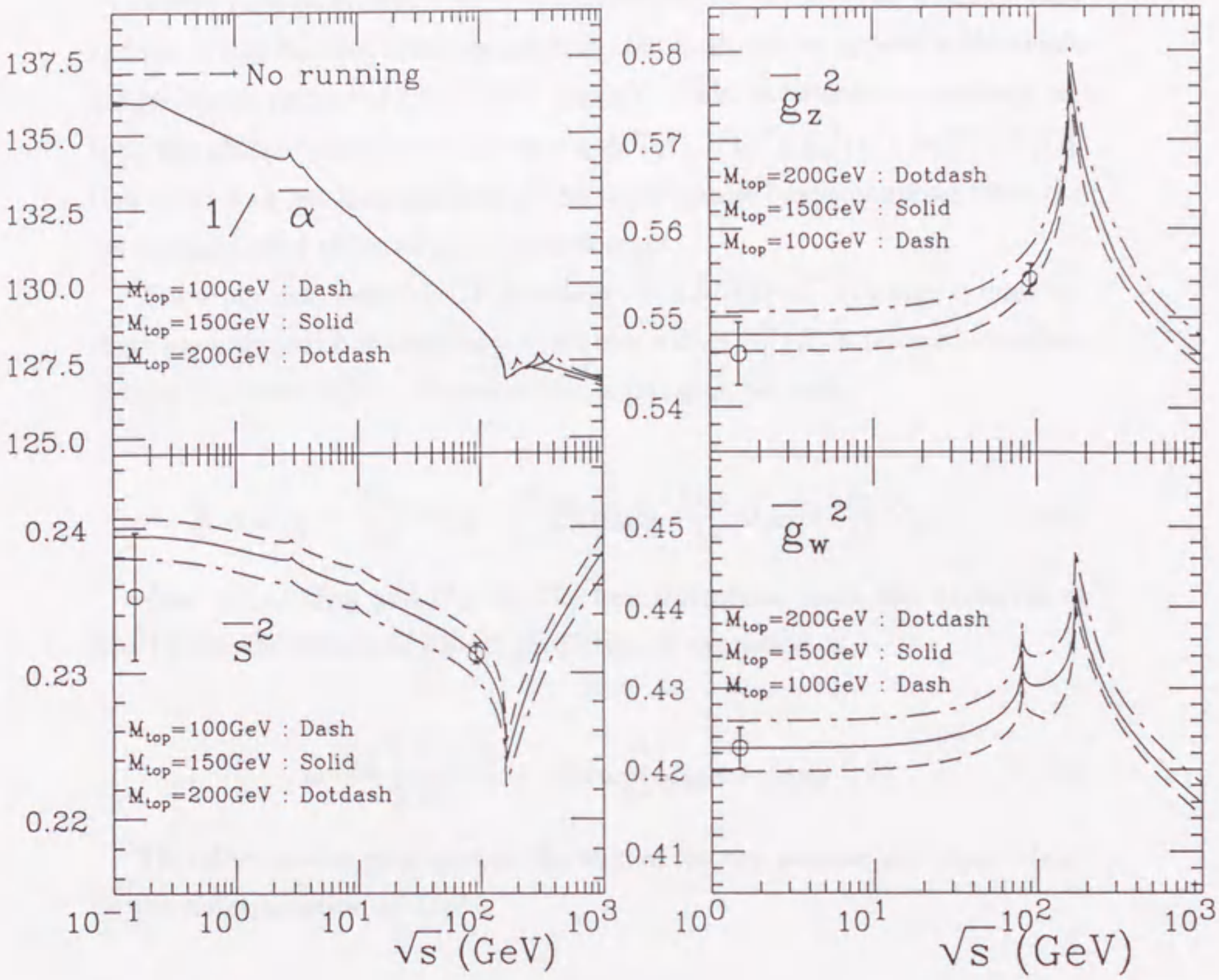


Figure 4: $\sqrt{s}$ dependence of the four effective form factors. The drown lines show the SM prediction. The white circles with error bars denote the results from LEP and low energy experiments.

If new physics interactions exists between the electroweak gauge bosons and the Higgs doublet fields, anomalous couplings can be appear in the triple gauge boson vertex($\gamma/Z^0$-$W^+W^-$ vertex). This anoumolous couplings affects the oblique parameters like $\bar{\alpha}(q^2)$, $\bar{g_z}^2(q^2)$, $\bar{s}^2(q^2)$, $\bar{g_w}^2(q^2)$, or $S$,$T$,$U$[12]. Hence, we can get informations of the triple gauge boson coupling from the determination of these effective form factors.

If new physics conserves CP invariance and $SU(2)\times U(1)$ gauge symmetry, there are only four 6-dimensional operators with $\gamma/W/Z/o$ fields which affect oblique parameters[37]. Therefore the lagrangian becomes,

$$\mathcal{L} = \mathcal{L}_{SM} + \frac{f_{DW}}{\Lambda^2}O_{DW} + \frac{f_{DB}}{\Lambda^2}O_{DB} + \frac{f_{BW}}{\Lambda^2}O_{BW} + \frac{f_{o1}}{\Lambda^2}O_{o1} \tag{10}$$

$O_{DW}$, $O_{DB}$, $O_{DB}$ and $O_{o1}$ are the four operators. And, the deviation of $\bar{\alpha}(q^2)$ from the Standard Model prediction is expressed as,

$$\triangle\frac{\bar{\alpha}(q^2)-\bar{\alpha}(0)}{\bar{\alpha}(0)} = -8\pi\alpha\frac{q^2}{\Lambda^2}(f_{DW}+f_{DB}) \tag{11}$$

Therefore we can give limit on the sum of the two parameters ($f_{DW}+f_{DB}$) by the determination of $\bar{\alpha}(q^2)$.

## 2.5 S-matrix approach in $e^+e^- \rightarrow hadrons$

The parameters of $Z^0$ boson is well determined by the LEP experiments[13] with the following cross section formula:

$$\sigma_h = \sigma_{\gamma\gamma} + \sigma_{\gamma Z} + \sigma_{had}^{pole}\frac{s{\Gamma_Z}^2}{(s-M_Z^2)+(s^2/M_Z^2)\Gamma_Z^2} \tag{12}$$

The mass($M_Z$), width($\Gamma_Z$) and the cross section at pole($\sigma_{had}^{pole}$) were obtained by a model independent lineshape fit. In this scheme, the photon exchange($\sigma_{\gamma\gamma}$) and the interference term between photon and $Z^0$ ($\sigma_{\gamma Z}$) are assumed to be those of SM, because they are small ($\sim$0.3%) at LEP energy region. However, the interference term is proportional to the product of the electron and the final state fermions' vector couplings to the $Z^0$ boson. Therefore, in a fully model-independent way, at least the interference

between $\gamma$ and $Z^0$ should be regarded as a free parameter to determine $Z^0$ parameters. In order to realize it, the total hadronic cross section is expressed by the following formula in the S-matrix formalism[14, 15];

$$\sigma_h = \frac{4\pi\alpha}{3}[\frac{R_\gamma}{s} + \frac{sR}{(s-\bar{M}_Z^2)^2+\bar{M}_Z^2\bar{\Gamma}_Z^2} + \frac{(s-\bar{M}_Z^2)J_{had}}{(s-\bar{M}_Z^2)^2+\bar{M}_Z^2\bar{\Gamma}_Z^2}] \equiv \sigma^{smat}(s). \quad (13)$$

where the first and second terms are corresponding to $\gamma$ and $Z^0$ exchanges, respectively, while the last one is the interference between them. The conventional formalism using $s$-dependent width of $Z^0$ with $M_Z$ and $\Gamma_Z$ is relating to the S-matrix one by[17],

$$\bar{M}_Z = M_Z[1+\Gamma_Z^2/M_Z^2]^{-\frac{1}{2}} \approx M_Z - 34\mathrm{MeV}, \quad (14)$$

$$\bar{\Gamma}_Z = \Gamma_Z[1+\Gamma_Z^2/M_Z^2]^{-\frac{1}{2}} \approx \Gamma_Z - 1\mathrm{MeV}. \quad (15)$$

In this formula, there should be four free parameters of $\bar{M}_Z$, $\bar{\Gamma}_Z$, $R$ and $J_{had}$ assuming $R_\gamma$ is well known by theories. Among the four parameters $\bar{M}_Z$ has a strong correlation with $J_{had}$ as clearly seen in Eq.(13), while $\bar{\Gamma}_Z$ is strongly correlated with $R$ because the $Z^0$ pole cross section($\sqrt{s} = \bar{M}_Z$) is expressed by $R/\bar{\Gamma}_Z^2$. In the usual three parameter fit, however,the coefficient of the interference term ($J_{had}$) is given by the SM[15]. In fact, if we do not assume the SM for $\gamma$-$Z$ interference, the error of the $Z^0$ mass becomes as large as 15MeV[16]. Since the $\gamma$-$Z$ interference is expected to be as large as 3% of the total hadronic cross section at TRISTAN, this error can be reduced by a simultaneous fit to the total cross sections at the LEP and TRISTAN energies.

# 3 Experimental Apparatus

## 3.1 TRISTAN $e^+e^-$ collider

TRISTAN is a large $e^+e^-$ colliding beam accelerator at National Laboratory for High Energy Physics(KEK). It consists of three components. One is a 400m linear accelerator (LINAC) which accelerates electrons and positrons up to 2.5GeV and injects them into an accumulation ring(AR). The AR is a storage accelerator ring of 377m circumference. The electrons and positrons are stored in AR to sufficient currents and accelerated upto 8.0GeV. And then, they are injected into a main ring(MR). The MR has a circumference of 3018m and has four arc sections and four straight sections with interaction regions at their mid points. The electrons and positrons are accelerated to the required collision energy in the MR, and then the collision operation mode is turned on. The absolute beam energy was estimated to be 28886MeV from the RF frequency shift, and in 1992, it was measured by the spin depolarization method. The measured result was 28887.639±0.022MeV, which agreed with the expected value within 2MeV. Considering the variation of the MR condition through its operation, the absolute center mass energy at so called "58GeV operation" was estimated to be 57.77GeV[18]. The performance of the TRISTAN accelerator is summarized in Table 1. Fig.5 is the schematic view.

## 3.2 The TOPAZ detector

The TOPAZ detector is a general purpose magnetic spectrometer to study the charged and neutral particles produced by $e^+e^-$ annihilation. A schematic view of the TOPAZ detector is shown in Fig.6 and its performance is summarized in Table 2.

### Vertex Chamber

The vertex chamber(VTX) is a cylindrical jet drift chamber to detect particles with lifetimes of the order of a picosecond, by reconstructing the decay vertices. It was installed in the pressure vessel filled with the gas

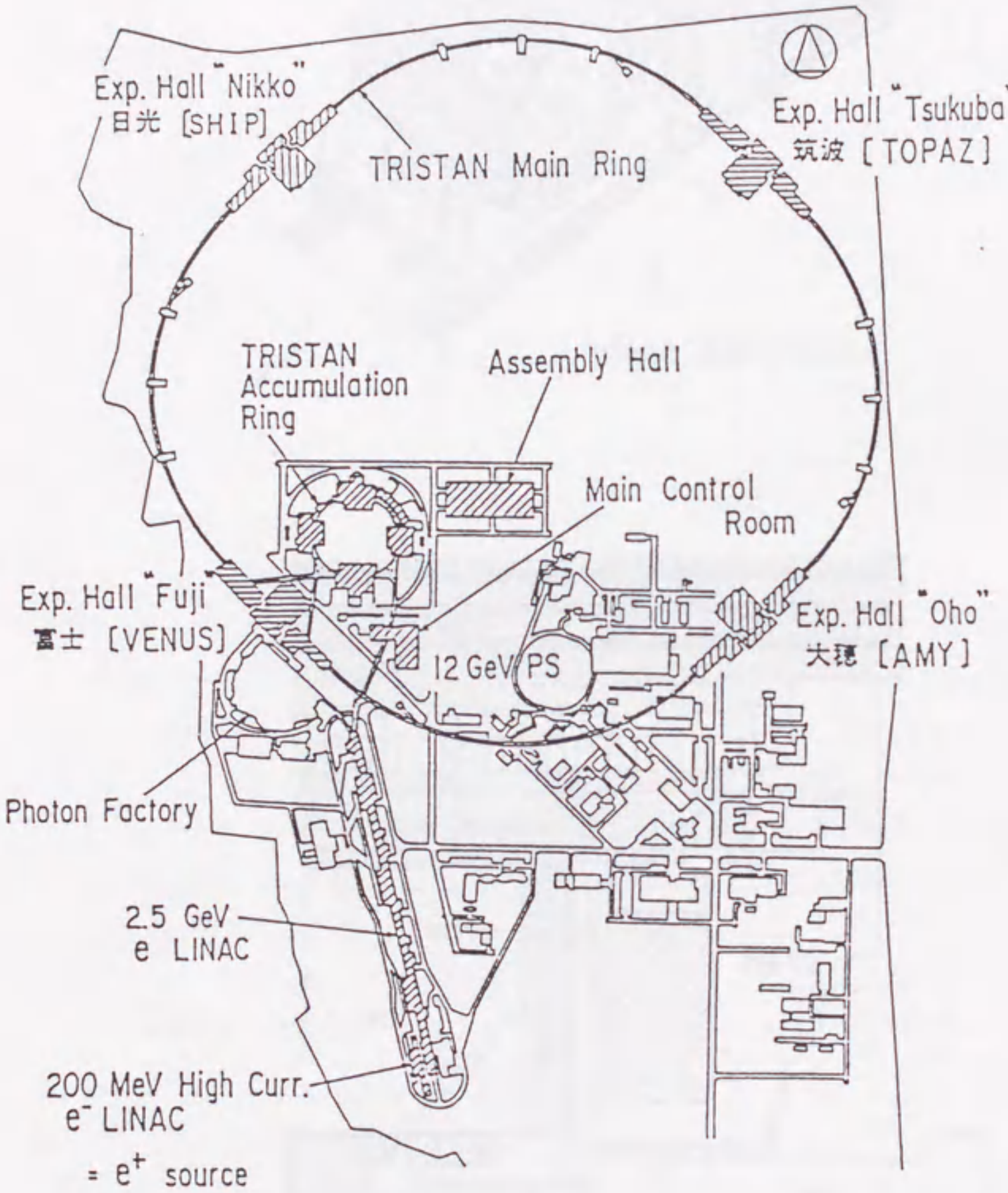


Figure 5: A schematic view of the TRISTAN accelerator

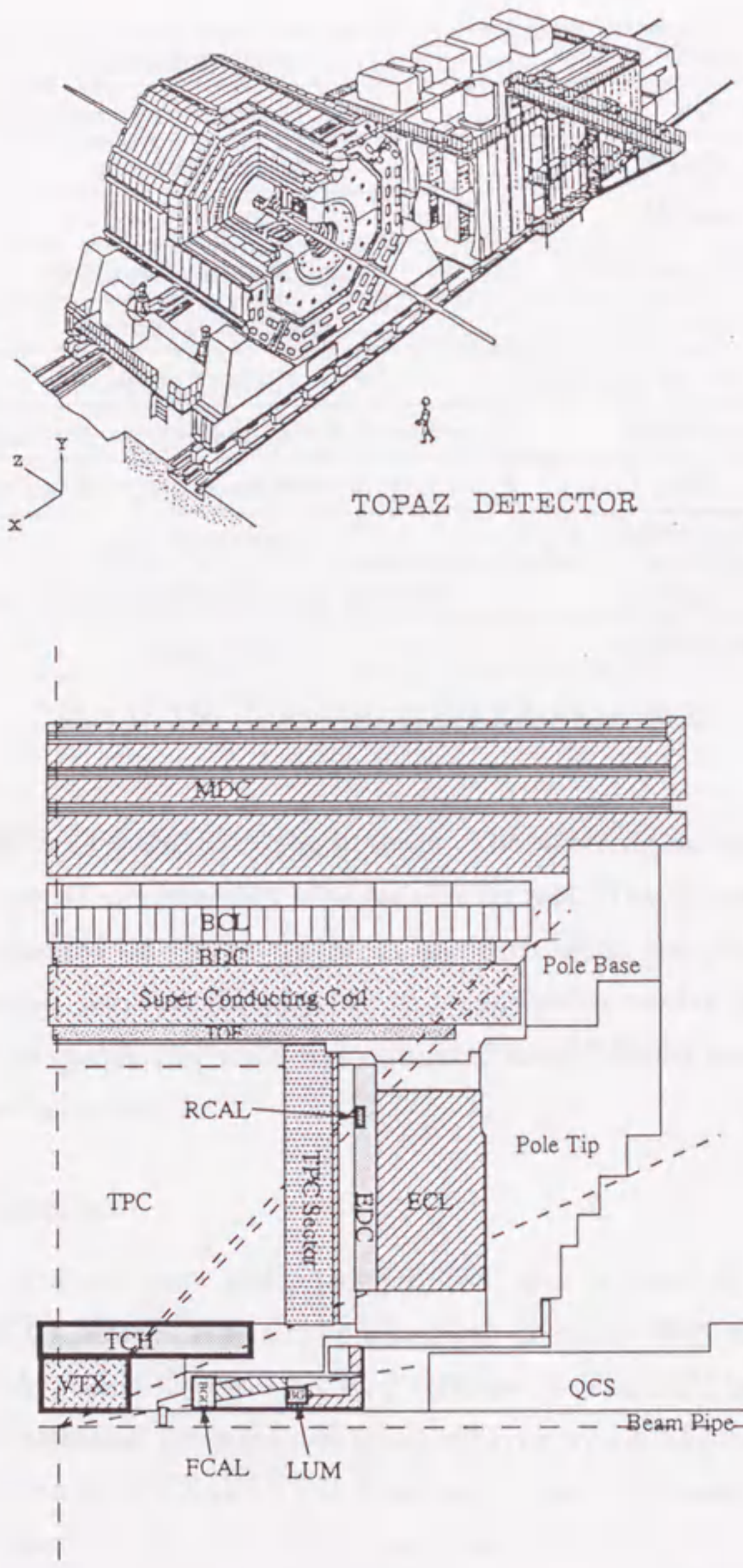


Figure 6: A schematic view of the TOPAZ detector

| | |
|---|---|
| circumference | 3.02 km |
| number of interaction points | 4 |
| injection energy | 8 GeV |
| max. energy | 32GeV |
| natural beam spreads | 0.0016 at 30 GeV |
| number of bunches | $2e^+ + 2e^-$ |
| beam current | 13.6 mA for 4 bunches |
| beta function at collision point(hor./ver.) | 10m/4cm |
| vertical-horizontal emittance ratio | 1.5% |
| peak luminosity | $1.4 \times 10^{31}$ cm$^{-2}$sec$^{-1}$ |
| max. integrated luminosity per day | 1.07pb$^{-1}$ |
| Beam life | 4~5 hours |

Table 1: The parameters of the TRISTAN MR.

mixture of 92% $CO_2$ and 8% $C_2H_6$ at 3atm. The water vapor was also mixed 320 ppm to avoid an instability of sense wire current. The fidutial volume of VTX is segmented into 16 sectors in $\phi$, and each sector has 25 sense wires. The sense wire plane is tilted by 16° to be enable to resolve the left right ambiguity. Its spatial resolution was estimated using Bhabha events, and $\sigma_{r\phi}$ = 38$\mu$m was achieved[19].

**Trigger Chamber**

At 1989, the old inner drift chamber(IDC) was replaced by the trigger chamber(TCH). The TCH is a cylindrical drift chamber filled with gas mixture of 89% Ar, 10% $CO_2$ and 1% $CH_4$ ("HRS gas"). The TCH has 8 measuring layers constructed by hexagonal small cell type wire configuration, and is located between the VTX and TPC. The charged pre-trigger signal was made by combination with the TCH wire hits and the Time-of-flight counter(TOF) hits by look-up-table method. The TCH also works as a tracking device with the spatial resolution of 250$\mu$m.

| Components | Material and Size | Measured Performance |
|---|---|---|
| Magnet | 2.9m($\phi$) × 5m (L) , 0.7 $X_0$ | B = 1.0 T |
| Beam pipe | 0.108m($\phi$) 3.0mm-thick Al<br>0.10m($\phi$) 1.3mm-thick Be<br>0.10m($\phi$) 5mm-thick Al | (from '89 fall till '90 summer)<br>($\|z\| \leq$15cm, after '90 fall)<br>($\|z\| \geq$15cm, after '90 fall) |
| VTX | 16 sectors, 25 measuring layers<br>$CO_2/C_2H_6$(92/8) $H_2O$ 320ppm 3.0 atm | $\sigma_{r\phi} = 38\mu$m |
| TCH | Cylindrical 8 layers<br>$Ar/CO_2/CH_4$(89/10/1) 1.0 atm | $\sigma_{r\phi} = 250\mu$m |
| TPC | 2.4m($\phi$) × 2.2m(L)<br>16 sectors<br>10 pad rows, 176 wires/sector<br>$Ar/CH_4$(90/10) 3.5 atm | $\sigma_{r\phi} = 230\mu$m<br>$\sigma_z = 380\mu$m<br>$\sigma(dE/dx) = 4.6\%$<br>$\sigma_{p_t}/p_t = \sqrt{(1.5p_t)^2 + 1.6^2}\%$ |
| TOF | Plastic scinti.<br>64 segments in $\phi$ | $\sigma_{time} = 220$ ps ( Bhabha ) |
| BDC | Streamer tube<br>4 layer (r$\phi$) | $\sigma_{r\phi} = 350\mu$m |
| EDC | Streamer tube<br>2 layers each in x and y. | |
| BMU | 3 layers (r$\phi$), 1 layer (z) | $\sigma_{r\phi} = 1$mm |
| BCL | Lead-glass (SF6W), 20 $X_0$ thick<br>4300 blocks<br>$\|\cos\theta\| \leq 0.82$ | $\sigma_E/E = \sqrt{(\frac{8.0}{\sqrt{E}})^2 + (2.5)^2}$ %<br>$\sigma_\theta = 0.38°$ |
| RCL | W-Si. sandwich | $\sigma_E/E = 20\%$ |
| ECL | Pb-PWC Sandwich<br>18 $X_0$ thick<br>$0.85 \leq \|\cos\theta\| \leq 0.98$ | $\sigma_E/E = 6.7$ %<br>( for 26 GeV electron )<br>$\sigma_\theta = 0.7°$ |
| FCL | Silicon strip<br><br>BGO, 21 $X_0$ thick | $\sigma_\theta = 0.003$rad. at FBC,<br>$\sigma_\theta = 0.0015$rad. at LUM<br>$\sigma_E/E = 5.0\%$ |

Table 2: The performance of the TOPAZ detector components.

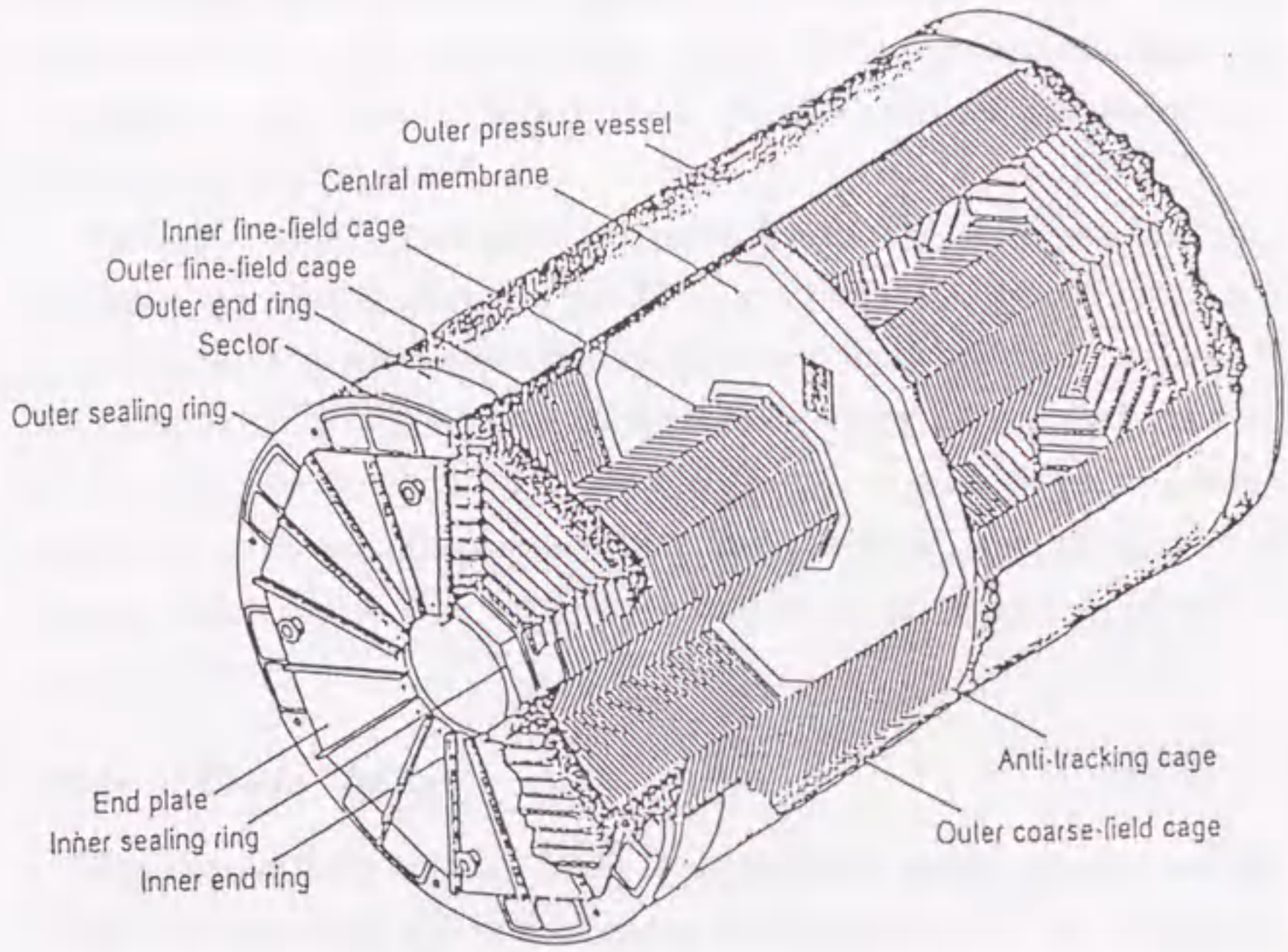


Figure 7: A bird's eye view of the TOPAZ TPC

### Time Projection Chamber

The time projection chamber(TPC) [20] is the central tracking device of the TOPAZ detector. A schematic view of the TPC is shown in Fig.7. The TPC is a three-dimensional tracking device which can identify particle species by energy deposit measurements having a fidutial volume of 2.4m in diameter and 2.2m axial length, and is filled with the gas mixture of 90% Ar and 10% $CH_4$ at 3.5 atm. Charged particles crossing the sensitive volume ionize gas molecules and liberalize electrons along its trajectories. These electrons drift in the electric field(354V/cm) toward the end plate of the TPC with a speed of 5.3cm/$\mu$s. The both end plate of TPC is constructed from 16 trapezoidal "sectors", each equipped with 175 sense wires and 10 rows of segmented cathode pads(Fig.8). The electrons finally arrive at the sectors, and induce

the signals by making avalanches. The signals from sense wires and the cathode pads are amplified and shaped by an analog electronics. They are then read out by the charge coupled device(CCD) digitizers sampling the wave-forms into 100nsec "backet" from which z-positions and energy loss informarions are extracted.

Since the positive ions move $10^4$ times slower than electrons, they may pile up in the fiducial volume of the TPC, as a result, the electric field might be distorted. This effect could distort the reconstructed tracks by as large as a few cm. In order to avoid such an effect, the gating grids are placed in front of the sectors as shown in Fig.9. Usually the gating grids closed to prevent positive ions from drifting back to the fiducial volume, and are opened by the pre-trigger signal. The condition to turn on the pre-trigger signal will be explained later.

### Time-of Flight Counter

The time-of-flight counter(TOF) is consisted of plastic scintillators segmented into 64 in the $\phi$ direction, and is located outside the TPC. The TOF measures the time-of flight of the charged particles and generated the charged pre-trigger signal combined with the TCH wire hit pattern.

### Barrel Drift Chamber

The barrel drift chamber(BDC) is located in front of the barrel calorimeter(BCL), and consists of four layers of limited streamer tubes. Each streamer tube is made of a conductive plastic tube with an anode wire . The BDC was designed to help identifications of electrons from photons and to improve the momentum resolution for charged tracks combined with the TPC track informations.

### Barrel Calorimeter

The barrel calorimeter(BCL) measures the energy of electromagnetically interacting particles. The BCL is composed of 4300 lead glass couters and has a cylindrical structure covering the angular region of $|\cos\theta|$ <0.82. A

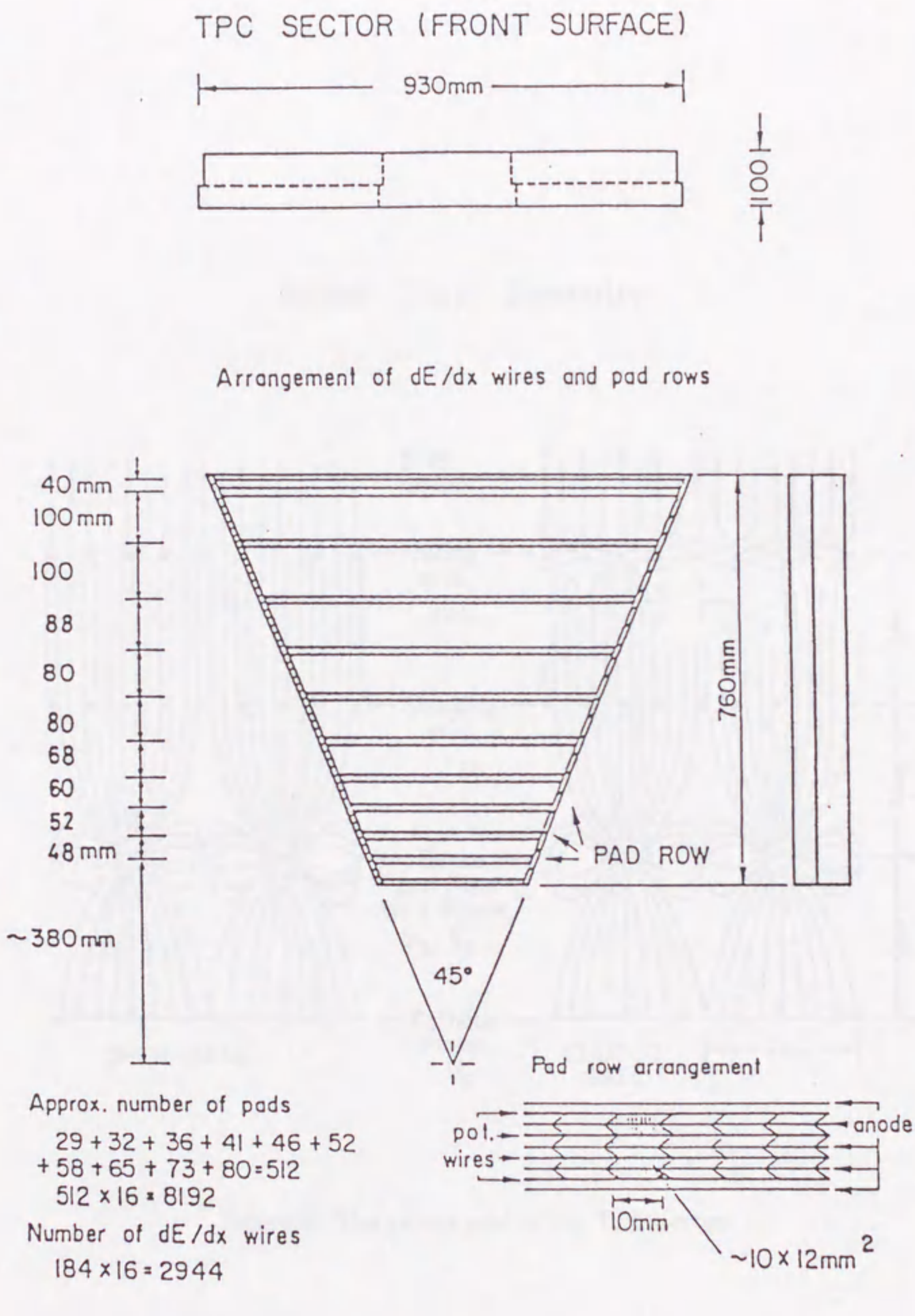


Figure 8: Front view and pad pattern of the TPC sector

Sector Wire Geometry

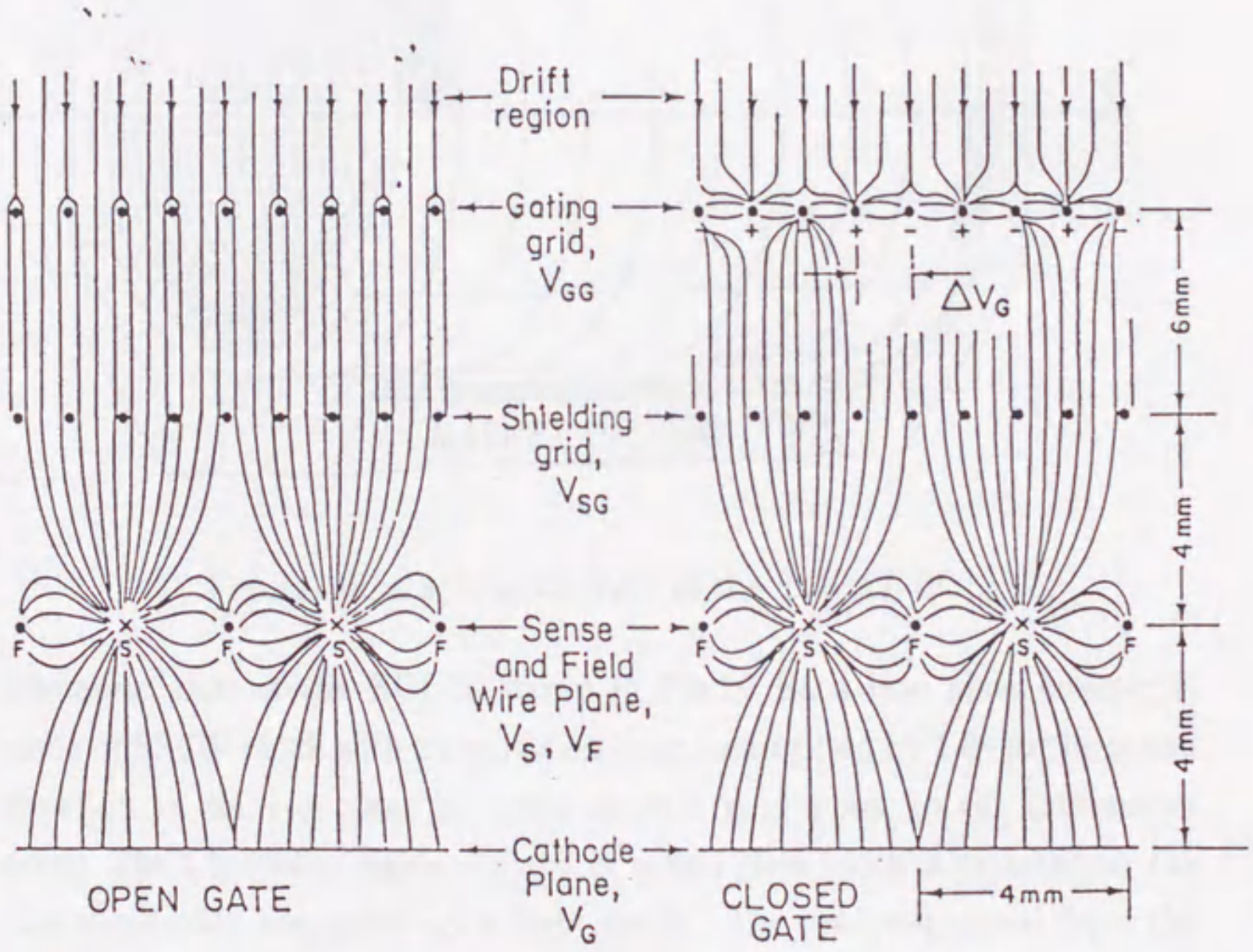


Figure 9: The gating grid of the TPC sector

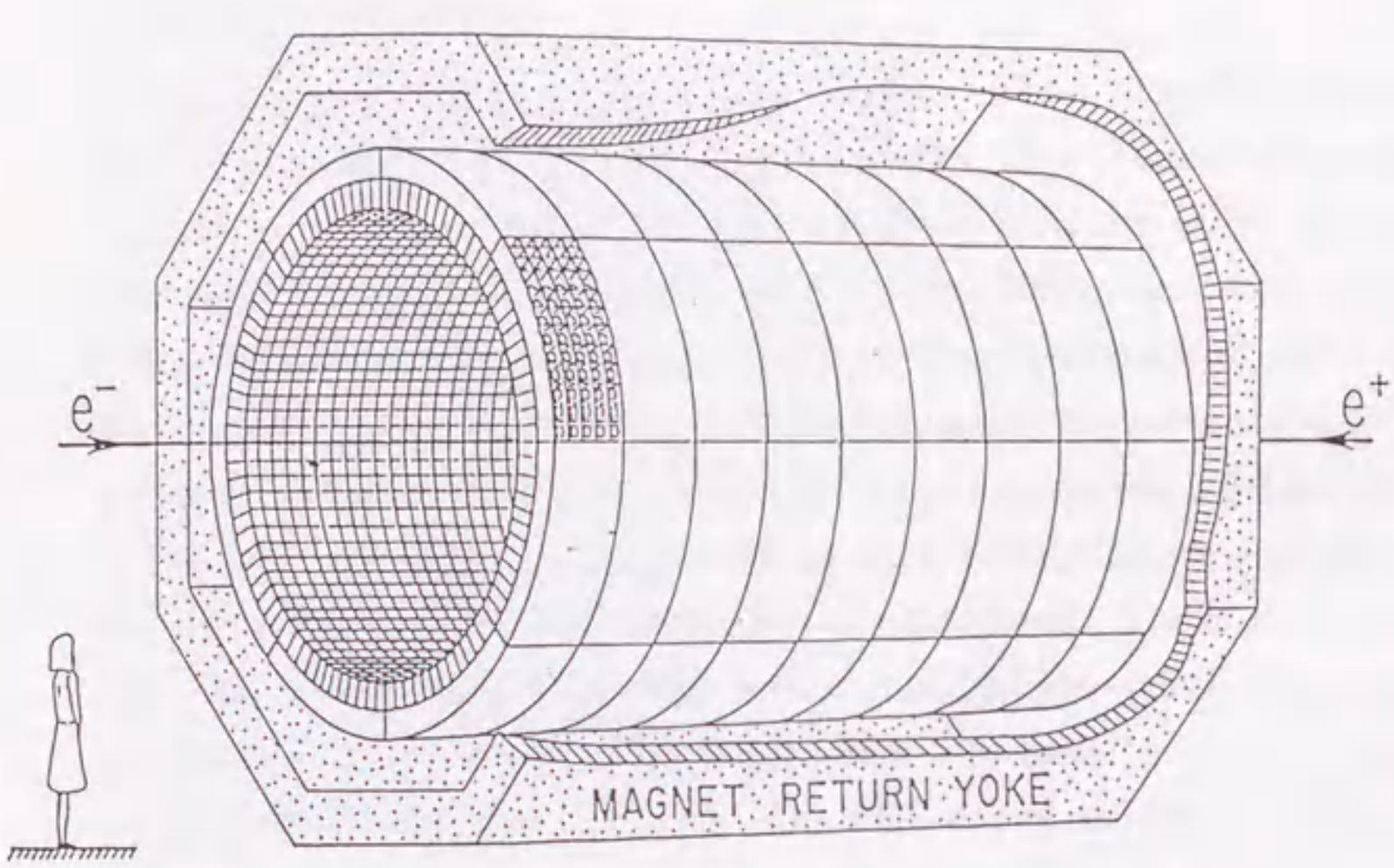


Figure 10: A schematic view of the TOPAZ BCL

schematic view of the BCL is shown in Fig.10 Each lead glass counter is made of SF6W block with 20 radiation length and tilted by 1.8° to the radial direction in the r-$\phi$ plane to avoid counter gaps point to the interaction point. The Cherenkov lights emitted in a lead glass block is detected by the photomultiplier connected by a light guide. The read out signal from the photomultipliers are digitized and used for energy trigger. The system is calibrated using a Xe flush lamp. The performance of the BCL was studied by Bhabha events and the energy and the angular resolution were estimated to be $\sigma_E/E=\sqrt{(8.0/\sqrt{E})^2+(4.5)^2}$ %. ($E$ in GeV) and $\sigma_\theta$=0.38° respectively.

### Muon Drift Chamber

The muon drift chamber(MDC) is the outermost component of the TOPAZ detector. It covers 66% of the $4\pi$ solid angle. and is comprised by 4 layers

of drift chambers and 2 layers of 30cm thick iron muon filters. Each layer of the drift chambers has 2 sense wire planes. The tracking efficiency is 89.5% for cosmic rays with the spatial resolution in the $r-\phi$ plane of $\sigma_{r\phi}$=1mm.

### Forward Calorimeter

The forward calorimeter(FCL) [21] consists of four identical modules. Two of them are placed at Z=±60cm, and called the " Forward-Backward Calorimeter (FBC)"; the remaining two at Z=±120cm are called the "Luminosity Monitor(LUM)". Each module is azimuthally segmented into 12 blocks made of a "BGO calorimeter" with its front face equipped with a 12-fold-radially-segmented "Si-strip" detector to measure the polar angles ($\theta$) of scattered electrons. The BGO calorimeter further comprises a 5.3mm thick tungsten(W) absorber(1.5 $X_0$), a 150mm thick BGO(Bismuth germanate : $Bi_4Ge_3O_{12}$) crystal(13.5 $X_0$) and two silicon photodiodes. The Si-strip detectors were manufactured from large area n-doped silicon wafers. The p-side comprises 12 strips whose width ranges from 5 to 8mm to keep the angular resolution($\Delta\theta/\theta$) less than 5%. The FCL covers an angular region of $3.6° < \theta < 13.6°$, and the integrated luminosity was determined by the small angle Bhabha events detected in the FCL with $\sigma_E/E$=5.0%.

### End-cap Calorimeter

On each end-cap, the end-cap calorimeter(ECL) is mounted. The ECL is a gas sampling calorimeter covering the angular region $0.85 \leq |\cos\theta| \leq 0.98$. It consists of 36 layers of lead radiator and proportional counters made of the conductive plastic tubes, and has $18X_0$ thickness. The proportional counters are filled with the gas mixture of 95% Ar and 5% $CH_4$, and their signals are read out by the cathode pads. The energy and angular resolution were studied by Bhabha events. $\sigma_E/E$=6.7% and $\sigma_\theta$=0.7° were achieved for the Bhabha events at $\sqrt{s}$=52GeV.

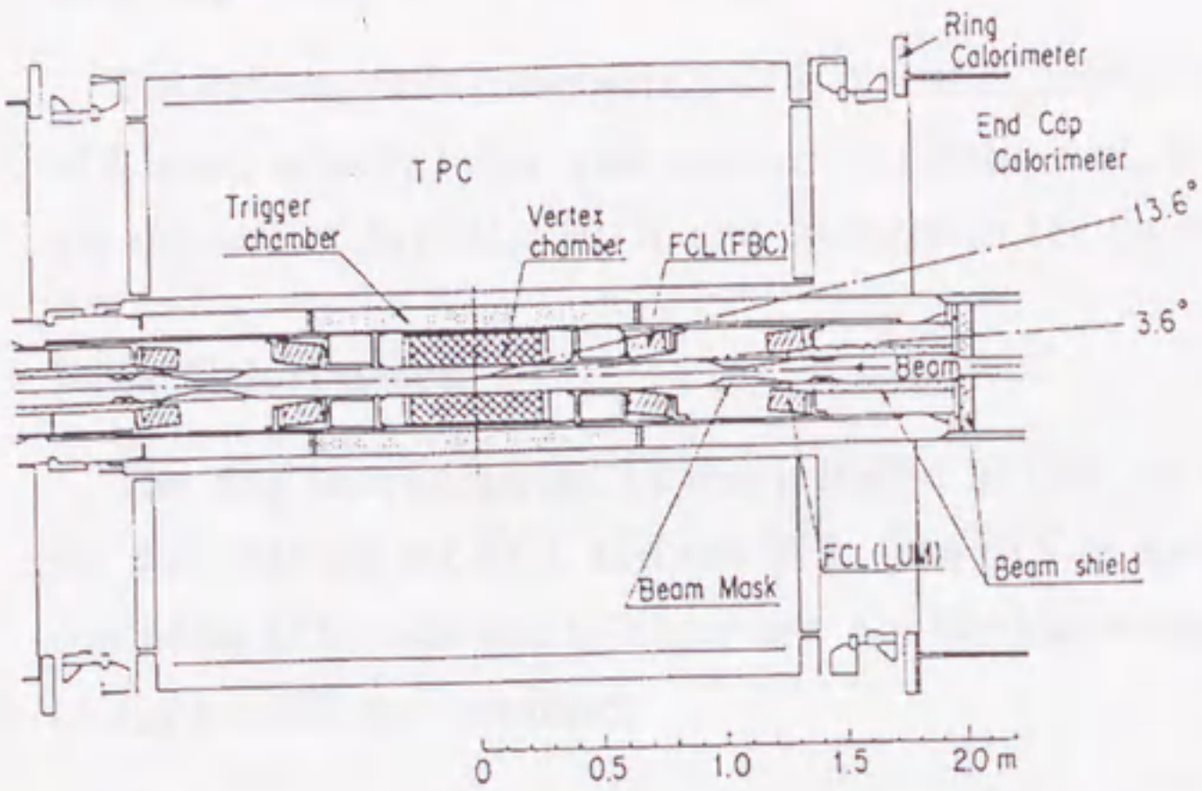


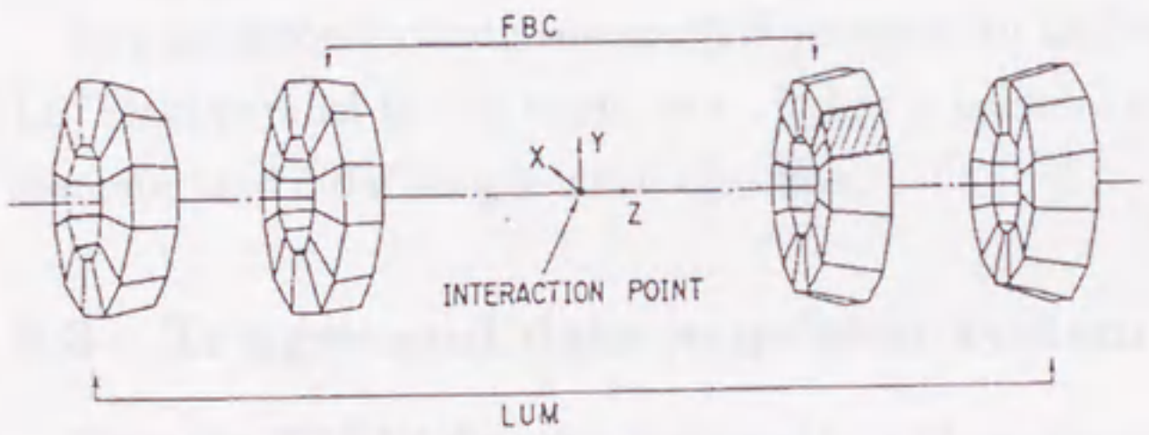


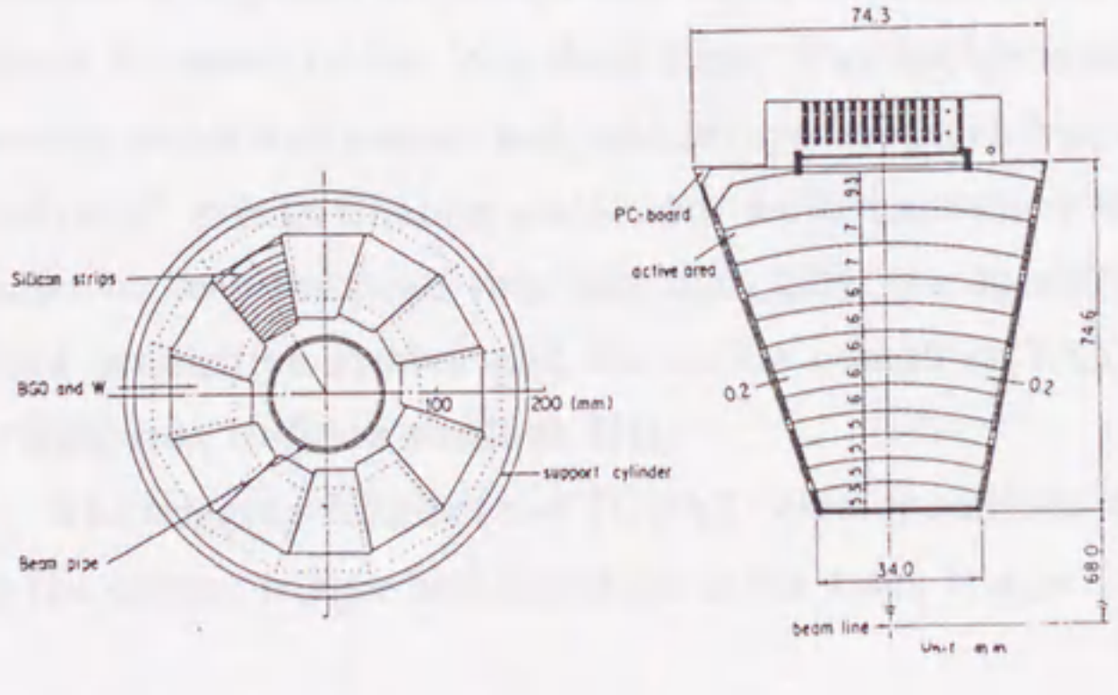


Figure 11: Views of the TOPAZ FCL in $r-z$ and $r-o$ planes. The Si-strip detector is also showed.

### End-cap Drift Chamber

The end-cap drift chamber(EDC) is placed in front of the ECL. It consists of 8 layers of drift tubes with conductive plastic wall. It was filled with the gas mixture of $Ar/CH_4$=80/20 and operated in the limited streamer mode.

### Ring Calorimeter

The ring calorimeter(RCL) was installed in 1989 on each end-cap to fill the gap between the ECL and the BCL. The RCL is a sampling calorimeter consisting of Si-pads and W absorbers. For Bhabha events, energy resolution of $\sigma_E/E$=20% was obtained.

### Superconducting solenoid

The superconductiong solenoid[22] provides an uniform magnetic field of 1.0 Tesla parallel to the beam axis. It has a cylindrical volume of 2.9m in diameter and 5.0m long in axial direction.

## 3.3 Trigger and data acquision system

Since the TOPAZ detector features the TPC as the main tracking device, it has the advantage of having the rich information from the TPC. However, 25msec is required to accept one event because of its large data size and hence it causes rather long dead time. The backgrounds such as beam gas events, beam wall events, and cosmic rays, are much frequent($\geq 10^4$) than the "physics" events(Bhabha scattering, multi hadronic events, and so on). In order to keep the dead time less than 10%, the specifications of FASTBUS data acquisition system and the online computer(VAX11/780) require the trigger rate to be as small as 3Hz.

The trigger scheme of the TOPAZ detector consists of two branches. One is the energy trigger and the other is the track trigger.

### 3.3.1 Energy trigger

The energy trigger is generated by the energy sum of the BCL and the ECL, and is consist of the total energy trigger and the partial energy trigger.

The total energy trigger is generated when

1. The energy deposit in BCL is larger than 4GeV, or

2. The energy deposit in ECL is larger than 10GeV.

The threshold for BCL total energy trigger has been lowered to 2GeV since 1992 run to detect single photon production events. To avoid increasing the trigger rate which is mainly due to the cosmic rays, the software veto was installed. The veto signal is generated by the MDC hits using the look up table method.

The partial energy trigger is generated when

1. At least two out of three BCL segments have an energy deposit larger than 1GeV, or

2. The shower energy in each end of ECL is larger than 3GeV, or

3. The shower energy in a ECL segment is larger than 3GeV and in a BCL segment is larger than 1GeV.

A typical trigger rate during beam run was 1.4Hz.

### 3.3.2 Track trigger

The track trigger is generated through two steps called charged pre-trigger and TPC trigger. The charged pre-trigger decision is done within 1.0$\mu$s to open the TPC gating grid using TCH and TOF hit pattern. The requirements are $p_t \geq$0.8GeV and maximum opening angle among the tracks >45° in the $r-\phi$ plane. The charged pre-trigger rate is 10$\sim$100Hz depending on the experimental condition.

The TPC trigger decision is done within 30$\mu$s by checking event vertex by the innermost 88 sense wire signals. An event is accepted if the vertex is within $\pm$20cm from the interaction point in the z direction.

### 3.3.3 Data acquisition system

Analog signals from the detector are sent to CAMAC or FASTBUS system and digitized. When the event satisfy the trigger condition, the digitized data

are collected by an online computer VAX11/780. The data are arranged into the raw data format, and are transferred to a central computer Fujitsu M-1800. The online computer and the central computer is linked by the optical fiber cable via VME channel interface. The monitored environmental condition such as tempreture, chamber gas pressure, gas flow rate, supplied high voltage, currents and magnetic field are also transferred to the central computer and stored in the event record. The FCL data are independently taken by a microcomputer $\mu$PDP. The luminosity is monitored in real time, and transfered to the online computer.

# 4 Data processing

The raw data from the online computer transferred to the offline computer are temporarily stored in the disk of the offline computer and copied to the auto-loading magnetic tapes after formatting process. We need to reconstruct position, time and four momentum of the detected particles. The procedure to reconstruct these observables of the particles is comprised by the two steps; "reduction" and "production".

## 4.1 Reduction step

In the reduction step, the data of each channel is corrected by the prepared calibration constants, and then is translated into energy and time. The sequence of the data is rearranged according to the geometrical structure of the detector. After that, we discard the junk events such as beam-gas events or beam-wall events to save tape volume and CPU time of the production step. The above procedure reduce the data size down to 1/3 of the raw data.

## 4.2 Production step

In the following, somewhat detail of the method of the track reconstruction in TPC and energy cluster reconstruction in BCL are described, since TPC and BCL are used to select hadronic events. TPC measures both the momentum and the energy deposit($dE/dX$) of the charged particles, but the identifications of particle species with $dE/dX$ measurements were not used in this analysis. Thus we skip to describing the $dE/dX$ measurements.

### 4.2.1 TPC track reconstruction

The charged tracks passing the sensitive volume of the TPC was mainly reconstructed by the signals induced on the cathode pads. The whole procedure of the TPC track reconstruction consists of space point making, track finding and track fitting. At first, z-position of a hit on a pad is obtained from the drift time information. If the neighboring pads have the same z-position, they are merged into a pad cluster. Fitting of the shared pulse

hight distribution in a cluster gives us the hit coordinate pararell to the pad row. The several wire hits associated to a pad row hit are fitted to obtain the coordinate perpendicular to the pad row. Consequently we obtain three dimensional space points information from the pad hits.

In the step of track finding, we pick up clusters of space points from a two dimensional histogram in the $\phi$-$z_{ref}$ plane. $z_{ref}$ is defined by

$$z_{ref} = z \times \frac{R_{ref}}{R} \tag{16}$$

where $R_{ref}$ is the radial position of the fixed reference point and $R$ is the radial position of the space point. A high momentum track make a small cluster of space points in $\phi$-$z_{ref}$ plane. Wider window in making a cluster accepts lower momentum tracks.

Finally, the space points found in a cluster(track candidate) are fitted to a helix. Shown in Fig.12, our helix parameterization is

$$\begin{aligned} x &= x_0 + d_\rho \cos\phi_0 + \frac{1}{\kappa}[\cos\phi_0 - \cos(\phi_0 + \phi)] \\ y &= y_0 + d_\rho \sin\phi_0 + \frac{1}{\kappa}[\sin\phi_0 - \sin(\phi_0 + \phi)] \\ z &= z_0 + d_z + \frac{\beta}{\kappa}\phi \end{aligned} \tag{17}$$

The five parameters($d_\rho$, $\phi_0$, $\kappa$, $d_z$ and $\beta$) are obtained by the fit. Used space points are poisoned, and next track finding processes are repeated.

### 4.2.2 BCL cluster reconstruction

Electrons and photons make showers in the calorimeter, and each shower extends to several counters. We must reconstruct energy clusters to know the energy of the incident electrons or photons. The clustering algorithm can be summarized as follows.

- Find out the counter($B_1$) with the highest energy($E_1$) among the counters having energy deposits larger than a threshold($E_{TH}$).
- Pick up the neighboring counters($B_2$'s) of $B_1$. Energy deposit $E_2$ on $B_2$ is added as a same cluster including $B_1$.

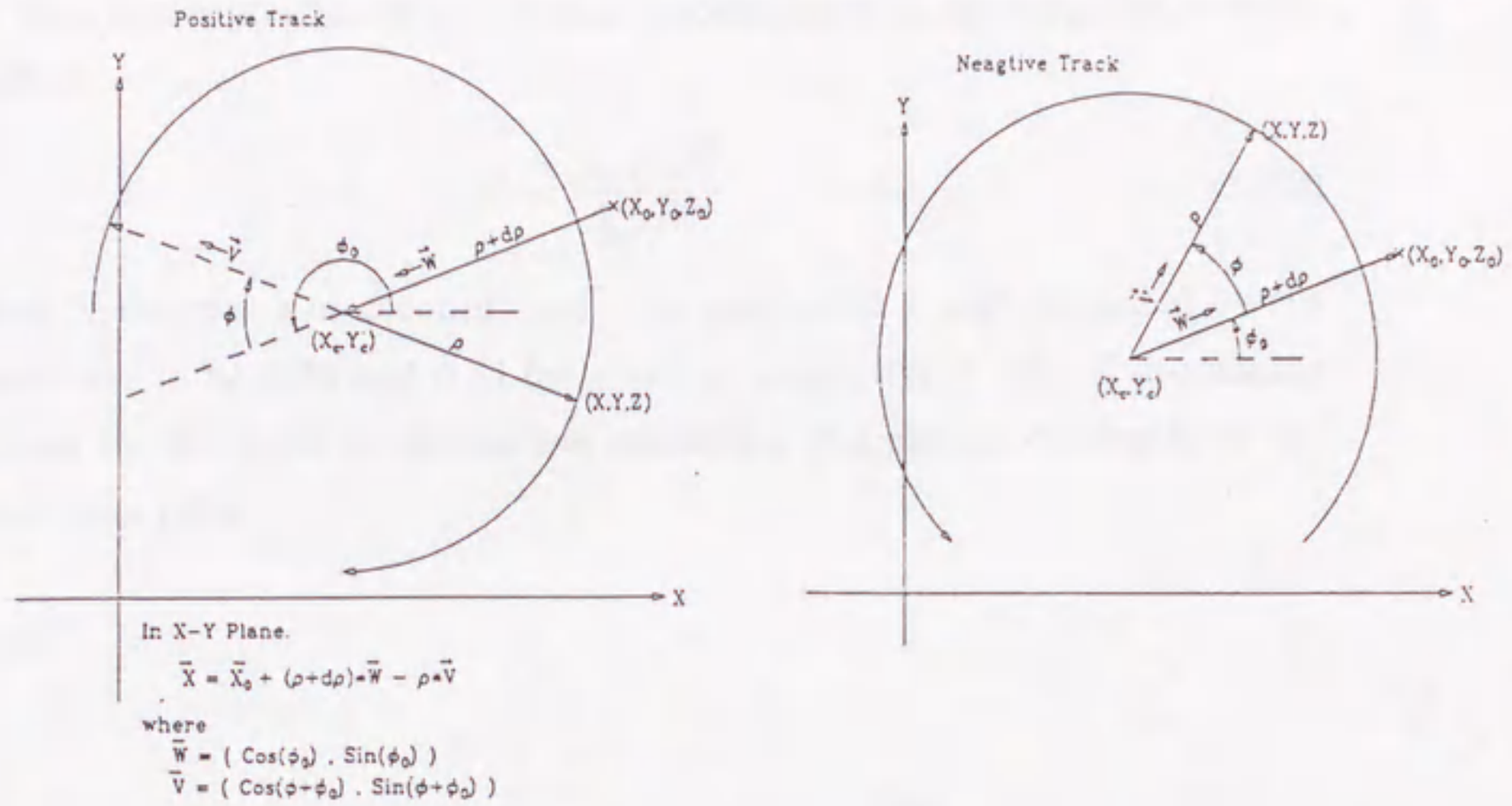


Figure 12: The helix parameterization in track reconstruction at TPC

- Pick up the neighboring counters($B_3$'s) of $B_2$. If its energy($E_3$) satisfies the following condition:

$$E_2 > C_1 E_{B_1}$$

or

$$E_{B_3} > C_2 E_{B_1} \quad \text{and} \quad E_{B_3} < C_3 E_{B_2} \tag{18}$$

then this $B_3$ is added to the same cluster. where $C_1$, $C_2$ and $C_3$ are constants which should be optimized.

- Regarding $B_3$ as $B_2$, repeat the step 3.

- Repeat the above procedure until all the counters having the energy deposits larger than $E_{TH}$ are arranged into each cluster.

The threshold energy($E_{TH}$) is fixed at 45MeV. Using Monte carlo simulation, the constants $C_{1,2,3}$ were optimized to be $C_1 = 0.65, C_2 = 0.08, C_3 = 1.20$.

The cluster position in $z-o$ plane is calculated by the weighted average method:

$$X = \frac{\sum_i X_i E_i^p}{\sum_i E_i^p} \tag{19}$$

where $X$ denotes $z$ or $\phi$ coordinate. The parameter $p$ was optimized by the simulation to be 0.26 and 0.34 for $z$ and $\phi$, respectively. The $R$ coordinate is given by the depth of the shower maximum of a photon coming from the interaction point.

# 5 Total hadronic cross section measurement

In this section, measurement of the total hadronic cross section is described. We explain criteria for hadronic event selection and the Monte Carlo event generation and detector simulation. In the way to derive the total hadronic cross section, background estimation, event selection efficiency, luminosity measurement and the QED correction are also described.

## 5.1 Event selection

We selected hadronic events in $e^+e^-$ annihilation using the TPC and the BCL. Our selection criteria were as follows:

1. The number of good tracks had to be $\geq 5$, where a good track was required to have

   - a transverse momentum to the beam axis larger than 150 MeV.
   - a distance of closest approach to the beam axis(z) less than 5cm in the xy-plane, as well as in the z-direction, and
   - a polar angle satisfying $0.02 \leq |\cos\theta| \leq 0.77$ to be well-contained in the detector.

   In order to reduce systematic error, only the tracks well-contained in the detector were used for event selection. Small $|\cos\theta|$ region were also rejected because tracks in this region were affected by the central membrane material.

2. The visible energy ($E_{vis}$) had to be larger than the beam energy ($E_{beam}$), where $E_{vis}$ was the sum of the momenta of the good tracks and the energies of BCL clusters of $E_{BCL} \geq 0.1$GeV.

3. The longitudinal momentum balance $|\sum P_z|/E_{beam} \leq 0.4$, where the $P_z$'s were longitudinal momenta of the good tracks or longitudinal energies of the BCL clusters.

4. The larger of the hemisphere invariant masses had to be$\geq$ 2.5GeV, where the two hemispheres were separated by a plane perpendicular to the thrust axis.

5. The events having two large clusters in BCL which exceeds $0.5E_{beam}$ were discarded to reject Bhabha backgrounds.

6. If a cluster larger than $0.7E_{beam}$ was found, these events were discarded in order to reject hard photon radiation from initial state(additional large cluster cut).

After these cuts were applied simultaneously, 9146 hadronic events remained for further analysis.

## 5.2 Monte carlo simulation

In order to estimate the selection efficiency and background events, Monte Carlo simulations are indispensable. Because we must know the real condition of the experiment and remove the detector-specific corrections to obtain the detector-independent results. The Monte Carlo simulations has the two steps. The first step is the event generation which generates the four-momentum of final state particles including radiated photons in accordance with the SM differential cross sections. The second step is the detector simulation propagating particles in the detector and simulate the detector response. After these two steps, we know the details of experiment by the event reconstruction using the simulated detector signal.

### 5.2.1 Event generation

We used the KORALZ3.8[23] and LUND6.3[24] programs as a generator of hadronic events. As described in the section 2, there are three processes of corrections contributing to the multihadron production in $e^+e^-$ annihilation; the weak corrections, the QED corrections and QCD corrections. The KORALZ program produces quark anti-quark pair and radiated photons based on the calculation using its subparts, DIZET3.01[8] program and YFS2[25] program for the weak corrections and the QED corrections, respectively. The

YFS2 program features the multiphoton bremsstrahlung out of the initial state beams. The contributions of soft photons are summed up to an infinite order using Yennie-Frautschi-Suura method(YFS exponentiation)[26].

The evolution of quark anti-quark pair into multi hadron final state comprises the two steps; the parton shower and fragmentation. In this analysis, these processes were calculated by the LUND6.3 parton shower and string fragmentation model. The parton shower method generates cascade showers of quarks and gluons, where each parton evolves two partons($q \to qg$, $g \to gg$, $g \to \bar{q}q$). This calculation describes the processes in which the quark or anti-quark or both radiate gluons, and the radiated gluons may radiate another gluons or turned into another quark anti-quark pair. The branching probability of partons are calculated in the leading log approximation(LLA) of the perturbative QCD, as given by Altarelli-Parisi equations[27]. The development of these cascade process are controlled by a cut-off value of parton virtual mass, $Q_0$. and the scale parameter $\Lambda$. And then, according to the string fragmentaion model, generated partons form hadrons via the breaking of the color flux that is stretched between opposite color charges.

### 5.2.2 Detector simulation

The generated particles were traced through the detector by TOPAZ simulator. This simulator code accounts all the conceivable effects such as interactions between the particles and detector materials and detector response. The structures and materials are precisely coded in the program and each particle is propagated by a small step from the interaction point.

In the TPC region, energy loss of the charged particles in the gas were calculated according to an empirical formula. The energy loss was smeared to be consistent with the Landau fluctuation observed by experiment. The smeared energy loss was translated into the pulse hight in each time bucket.

To simulate electromagnetic shower in the material, the EGS code[28] is widely used. In order to keep the accuracy of the simulation, the cut off energy in the EGS program must be sufficiently low. Therefore, tremendous amount of CPU time is required for this procedure. In the BCL, instead, the Bootstrap[29] method is used to simulate electromagnetic shower. This

method divide calorimeters in cells of suitable size and utilizes pre-generated showers("frozen shower") to get shower density. The cell size was optimized for the BCL to be 1.5cm in longitudinal(shower axis) and 0.5cm in the lateral direction. By replacing the EGS calculation with the frozen shower when the energy of the particle in the shower becomes lower than the cut-off, the CPU time was substantially reduced keeping the accuracy of the shower simulation.

The hadronic interactions were simulated by the GEISHA-7[30], and the short lived particles such as $\pi^0$, $K_s$ and $\Lambda$ were decayed in the simulator keeping the secondary vertex information.

For precision measurements, reliable efficiency and background estimations are crucial. This require a good agreement between the data and the Monte-Carlo simulations. Here, we compared the experimental distributions of key variables with the Monte-Carlo expectations in order to demonstrate the validity of our simulation. In the comparison, we applied all of the cuts except for the one concerning the quantity in question.

Figure 13(a) shows the multiplicity distribution of the good tracks (points with error bars) to be compared with the solid histogram, which is the Monte-Carlo expectation consisting of both the signal and the background. The dashed histogram in the same figure is the sum of all the considered background contributions, which is clustered in the low-multiplicity region and is dominated by $\tau$ pair events (shaded histogram). The discrepancies at the lowest two bins are mostly due to cosmic-ray, $e^+e^- \to \mu^+\mu^-(\gamma)$, and $e^+e^- \to e^+e^-l^+l^-$ events, which were not included in our Monte-Carlo simulations, since they were negligible small after cut (1). The agreement between the data and the Monte-Carlo prediction is reasonably good above the selection cut indicated in the figure, and this justifies the use of the Monte-Carlo simulations for both acceptance and background estimations. Figure 13(b) shows the distribution of the visible energy. The Monte-Carlo prediction (solid histogram) sufficiently well describes the data (points with error bars) above the cut indicated in the figure. The dashed histogram again represents the background, which is dominated by two-photon events in the low-$E_{vis}$ region and by $\tau$ pair events in the high-$E_{vis}$ region. The same kind of observation can be made for Figs.13(c) and (d), which are the distributions of

the $P_z$ balance and the larger hemisphere mass, respectively. Notice. in particular, that the background (dashed histogram) in Fig.13(d) comes mainly from $\tau$ pair events to which cut (4) is useful.

## 5.3 Derivation of the total hadronic cross section

From the number of the selected events ($N_{obs}$), the total hadronic cross section can be derived using the relation

$$\sigma_h = \frac{N_{obs} - N_{BG}}{L(1+\delta_{QED})\varepsilon}, \tag{20}$$

where $L$, $1+\delta_{QED}$, $\varepsilon$, and $N_{BG}$ are the integrated luminosity, the QED correction factor, the efficiency, and the number of estimated background events, respectively. The each terms are described in this section.

### 5.3.1 Background estimation

The selected events contain some backgrounds. The main sources of them were $\tau$ pair production and two-photon events.

For an estimation of the $\tau$ pair background, we generated $4 \times 10^4$ events using the full electroweak calculation of $O(\alpha)$ which was used in our published lepton-pair production analysis[31]. The contributions from two-photon events were estimated based on the Monte Carlo simulations used in our photon structure function measurement[32] and the inclusive jet measurement[33] for single-tagged and anti-tagged events, respectively. The Fig.14 shows the processes included in these Monte Carlo simulations for two photon events. The direct process(a) is a reaction of QED $O(\alpha^4)$, the one-resolved(b) and the two-resolved(c) photon process is due to the gluon constituents in the photon. The vector meson dominance model(VDM) is shown in (d). Together with other less-important background processes, their contributions are summarized in Table 3, which were subtracted as in Eq.(20).

### 5.3.2 Luminosity measurement

The integrated luminosity was measured by the FCL. Bhabha events for luminosity determination were selected based on the following criteria:

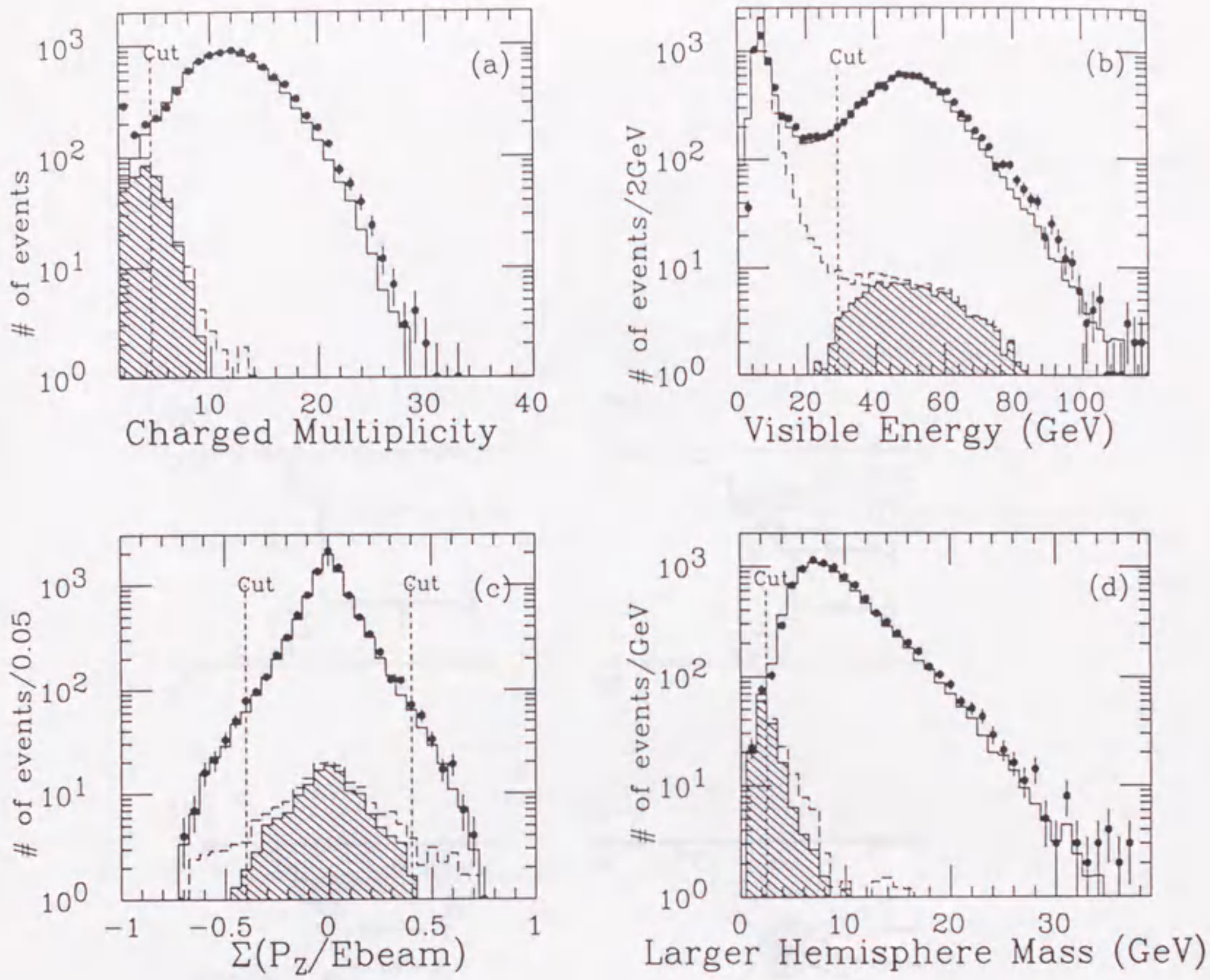


Figure 13: The key observables to select hadronic events.

| | | |
|---|---|---|
| Total observed events | | 9146 events |
| $\tau$ pair | | 98.9±2.5 events |
| Bhabha | | ≤3.8 events |
| $e^+e^- \to \gamma\gamma$ | | ≤ 0.7 events |
| Two photon | Anti tagged. | 7.3 events |
| | Single tagged. | 20.4 events |

Table 3: Physical backgrounds

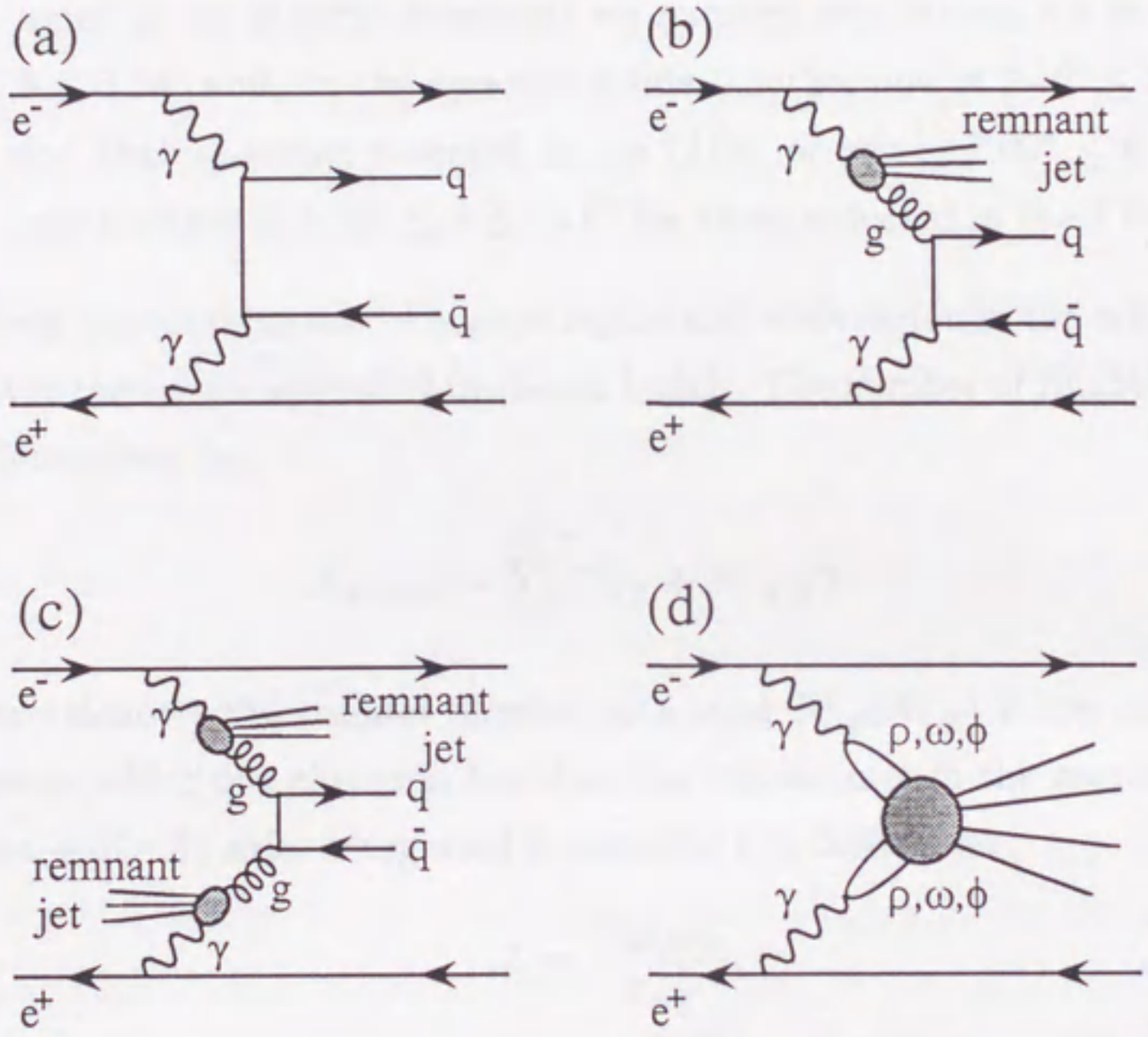


Figure 14: The processes in two photon events. (a) is the direct process, (b) and (c) are one- and two-resolved photon processes,respectively. The VDM is shown in (d).

1. There had to be two energy clusters, one in the forward and the other in the backward BGO calorimeters, each exceed 15GeV.

2. The difference in the azimuthal angles of the clusters determined by the BGO crystals ($\delta\phi$) had to satisfy $135° \leq \delta\phi \leq 225°$ in order for the clusters to be back-to-back in $\phi$.

3. The polar angles of the clusters were limited to be in the fiducial volumes of the Si-strip detectors: we required one Si-strip hit in $3.70° \leq \theta \leq 5.34°$ and, on the opposite z-side, another one in $3.46° \leq \theta \leq 6.3°$ for Bhabha events detected in the LUM, or one in $7.09° \leq \theta \leq 10.2°$ and another in $6.63° \leq \theta \leq 12.0°$ for those detected in the FBC.

We took the combination of narrow region and wide region in the criterion(3) to cover the spatial spread of the beam bunch. The number of Bhabha events are determined by,

$$N_{Bhabha} = \sum_{i}^{12} (N^{i}_{+Z} + N^{i}_{-Z})/2 \tag{21}$$

where $i$ denotes the counter number in $\phi$, and $N^{i}_{+Z}(N^{i}_{-Z})$ is the number of events in which one cluster is found at the i-th counter in the narrow region on the $+Z(-Z)$ side. Integrated luminosity $L$ is defined as ;

$$L = \frac{N_{Bhabha}}{\sigma_{eff}},$$
$$\sigma_{eff} = \sigma_{GEN} \frac{N^{MC}_{acc}}{N^{MC}_{GEN}} \tag{22}$$

where $\sigma_{eff}$ is the effective cross section determined by a Monte Carlo simulation: $\sigma_{GEN}$, $N^{MC}_{GEN}$ and $N^{MC}_{acc}$ represent the predicted cross section, the nunber of generated Bhabha events and the number of accepted events through the selection criteria, respectively. Bhabha events are generated by the full electroweak $O(\alpha)$ generator[34]. The integrated luminosity was determined to be $90.85 \pm 0.14(\text{stat}) \pm 2.27(\text{sys}) \text{pb}^{-1}$, whose systematic error in the luminosity measurement is described in the next section.

### 5.3.3 Radiative correction

In order to make the presented cross section model-independent or as much as possible, proper radiative correction should be made. Our main interest is the hard scattering process, which occurs in the short distance, described as the weak corrections. In order to extract it model-independently, we need to remove only the long distance physics effect. In actual, the removal of long distance physics is equivalent to applying the QED corrections and making the acceptance correction.

In the traditional way of TRISTAN experiments, the results were presented as the Born ("tree level") cross section using the full electroweak calculation. Since this scheme corrected the data with not only the QED corrections but also the weak corrections according to the SM, the presented results strongly depend on SM and its unknown parameters such as the masses of the top quark and the Higgs boson. Consequently, the obtained results could not be used to test the wider class of models of beyond the SM.

As mentioned in the previous section, the factor $1+\delta_{QED}$ comprises the model-independent QED corrections described in Ref.[3]. The $1+\delta_{QED}$ was calculated using KORALZ3.8[23] in the $O(\alpha^2)$+ exponentiation mode, which is the highest order calculation available at present. In this mode, the interference of the initial and final radiation is not taken into account. Although the interference affects the forward-backward asymmetry by the about of 1% for quark pair production, the contribution to the total cross section is expected to be negligibly small; estimated to be less than 0.06% in the $O(\alpha)$ mode. The resultant value of $1+\delta_{QED}$ is 1.193 for $k_{max} = 0.99E_{Beam}$, $M_Z$=91.187GeV, $M_{Top}$=174GeV, and $M_{Higgs}$=100GeV at $\sqrt{s}$=57.77GeV. Its dependence on the values of $M_{Top}$ and $M_{Higgs}$ was found to be less than the statistical error of event generation (0.1%). Another calculation of $1+\delta_{QED}$ was executed with the interference of the initial and final radiations using ZFITTER4.5[15], resulting in a $1+\delta_{QED}$ value of 1.193, which agrees with that determined by KORALZ3.8.

### 5.3.4 Detection efficiency

The generated events were processed through the TOPAZ detector simulator and the aforementioned event selection. Contrary to the situation of the LEP experiments at $Z^0$, we had a significant number of events discarded by either the visible energy cut [cut (2)] or the longitudinal momentum balance cut [cut (3)], due to undetected hard photons. The estimation of the photonic effects must be more carefully carried out in our case; although the $O(\alpha)$ corrections, containing hard photon radiation, dominantly affected the detection efficiency, higher order QED corrections increased $1+\delta_{QED}$ by 1%, through the effect of multiple emission of soft photons. We thus employed KORALZ in the $O(\alpha^2)+$ exponentiation mode as our event generator in order to estimate the efficiency ($\varepsilon$) together with $1+\delta_{QED}$. The parton showering and hadronization were carried out using LUND6.3[24] with the tuned parameters described in the next section. The generated events were processed through the TOPAZ detector simulator and the aforementioned event selection. The resultant efficiency was $\varepsilon$=57.93% at $k_{max} = 0.99E_{beam}$.

## 5.4 Systematic errors

### Luminosity measurement

At present, the largest source of systematic errors is the uncertainty in the integrated luminosity measurement by the FCL. The accuracy of the FCL construction and its relative positioning error from the beam line have been described in detail elsewhere[21]. The error of these geometrical origins was estimated to be only 0.45%. On the other hand, the systematic errors due to the uncertainties in the absolute energy scale of the BGO blocks and the efficiency of Si strips were estimated from the difference among the integrated luminosities measured in six angular regions: $3.7° < \theta < 3.9°$, $3.9° < \theta < 4.5°$, $4.5° < \theta < 5.0°$ in the LUM, $7.1° < \theta < 7.5°$, $7.5° < \theta < 8.6°$, and $8.6° < \theta < 9.6°$ in the FBC. The maximum difference was 2.2%. Including theoretical ambiguity[34], the total systematic error of the luminosity determination was 2.5%.

### Radiative correction

The $k_{max}$ dependence of $\varepsilon(1+\delta_{QED})$ was found to be less than the statistical error (0.3%) of the Monte-Carlo simulation: selection criterion (6) is expected to make negligible the effect of hard photon emissions. The other parameters dependence was already described in the previous subsections.

### Detector simulation

Any disagreement between the simulations and the data induces systematic errors in the estimation of $\varepsilon$. Here, we discuss the systematic errors introduced by small discrepancies noticeable in Figs. 13(a)~(d). The charged multiplicity distribution of the Monte-Carlo data showed a small offset with respect to that of the real data. There also seemed to be a systematic scale difference between the visible energy distributions of the Monte-Carlo and the real data. The errors in the efficiency estimation from these discrepancies were evaluated by calculating the efficiency after off-setting the Monte-Carlo charged-multiplicity distribution and rescaling the visible energy distribution of the Monte-Carlo data. We also checked, by rescaling, the error due to uncertainties of the longitudinal momentum balance and that due to energy scale ambiguities of the hard BCL cluster in cuts (5) and (6). Including the statistical error of the detector simulation ($10^5$ events), these errors amounted to a detector-induced systematic uncertainty of 1.5% in the efficiency. The error due to the larger hemisphere mass cut was estimated in a similar way and was found to be negligibly small.

### Fragmentation and hadronization

The error due to fragmentation and hadronization was also estimated. In this analysis, the fragmentation parameters ($b$, $\Lambda$, and $\sigma_q$) were detuned by $\pm 1$-$\sigma$ from the optimized values ($a$ was fixed at 0.361 because it strongly correlates with $b$, and the best-fit values of these three parameters were $b = 0.914 \pm 0.016$, $\Lambda = 0.378 \pm 0.010$GeV, and $\sigma_q = 0.355 \pm 0.005$GeV)[35]. The difference in the estimated efficiencies between the optimized Monte-Carlo simulation and the detuned one was 0.9%.

| | | |
|---|---|---|
| Luminosity | | 2.5% by FCL |
| Rad. correction | $M_{top}$,$M_{Higgs}$ dependence | $\leq$0.1% |
| | initial/final interference | $\leq$0.06% |
| Detector simulation | | 1.5% |
| fragmentation parameter | | 0.9% |
| Background estimation | | 0.3% |
| Total | | 3.1% |

Table 4: Systematic Errors

### Background estimation

As for the background estimation, the largest uncertainty came from two-photon processes, for which we conservatively assumed a 100% theoretical ambiguity. The error estimated this way was 0.3% at most. The uncertainty of the $\tau$ pair background was less than 0.1%.

Summing all of these systematic errors in quadrature, we obtained a total systematic error of 3.1%. The systematic errors are summarized in Table 4.

## 5.5 Results

The total hadronic cross section was obtained to be

$$\sigma_h = 143.6 \pm 1.5(\text{stat}) \pm 4.5(\text{sys}) \quad \text{pb} \tag{23}$$

after the QED corrections. This value is consistent with the Standard Model prediction of 142.2pb with $M_Z$=91.187GeV, $M_{top}$=174GeV, $M_{Higgs}$=100GeV, and $\alpha_s(M_Z^2) = 0.12$, where the QCD correction was calculated up to $O({\alpha_s}^3)$[36]:

$$1 + \delta_{QCD} = 1 + \alpha_s/\pi + 1.409(\alpha_s/\pi)^2 - 12.805(\alpha_s/\pi)^3 \tag{24}$$

# 6 Discussions

In this section, we discuss two model-independent analyses : determination of $\bar{\alpha}(q^2)$ and $\gamma$-$Z$ interference.

## 6.1 The determination of $\bar{\alpha}(q^2)$

As described in the section 2, the neutral current interaction is expressed by the three oblique parameters; $\bar{\alpha}(q^2)$, $\bar{g}_z^2(q^2)$ and $\bar{s}^2(q^2)$ corresponding to $\gamma\gamma$,$ZZ$ and $\gamma Z$ propagators, respectively.

We evaluate $\bar{\alpha}$ at $\sqrt{s}$=57.77GeV from the measured cross section by the following way. The contributions of the vertex and box corrections were subtracted in accordance of SM. Since these corrections are smaller than the oblique corrections, the effect of new physics to them can be neglected. We used $\bar{g}_z^2(q^2)$ and $\bar{s}^2(q^2)$ which was measured by LEP experiments assuming that their running is according to the Standard Model. And $\alpha_s(M_Z^2)$ is fixed to be 0.12.

The error of QCD correction is not so serious for $\bar{\alpha}(q^2)$ extraction. Because QCD correction factor $(1+\delta_{QCD}) \approx (1+\alpha_s/\pi)$, therefore if even assuming that $\delta\alpha_s/\alpha_s \cong 10\%$, $\delta(1+\delta_{QCD})/(1+\delta_{QCD}) \approx 0.4\%$. At TRISTAN, statistical error or other systematic errors are larger than this. In other words, the total hadronic cross section measurement is more sensitive to $\bar{\alpha}(q^2)$ than $\alpha_s$ determination.

Therefore multihadron production is suitable channel to derive $\bar{\alpha}(q^2)$ because of its higher statistics than the lepton pair production.

The obtained value is,

$$1/\bar{\alpha}(q^2) = 128.6^{+0.9}_{-0.8}(\mathrm{stat})^{+2.7}_{-2.5}(\mathrm{sys}) \quad \text{at} \ \ \mathrm{q}^2 = (57.77\mathrm{GeV})^2,$$

which is the first direct measurement of $\bar{\alpha}(q^2)$ at high energy.

As shown in Figure15(a), our result is in good agreement with the SM prediction of 129.47±0.10. The error of the prediction is caused by the calculation procedure: the numerical value of the virtual photon's hadronic vacuum polarization is calculated by integrating the measured total hadronic

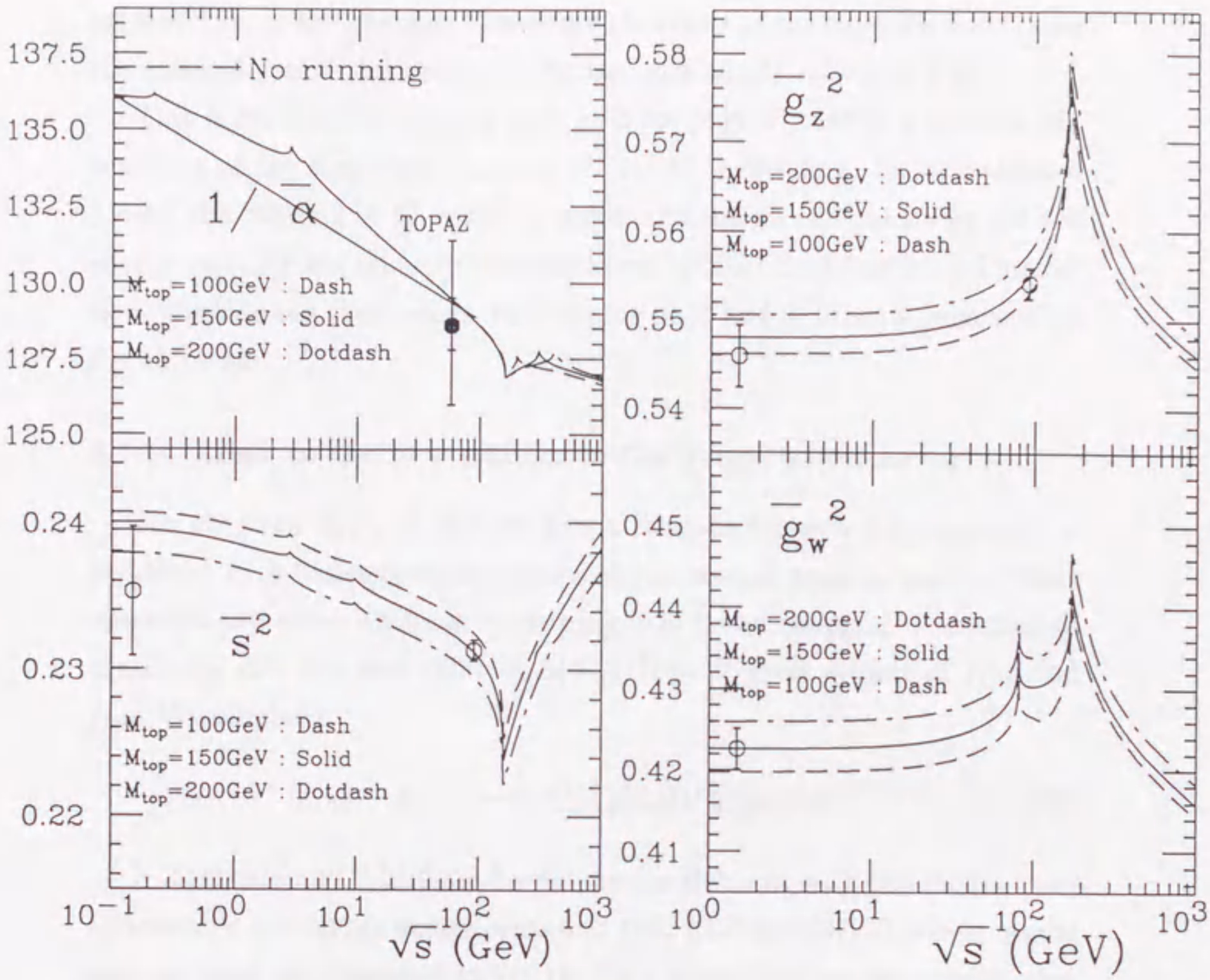


Figure 15: $\sqrt{s}$ dependence of the four effective form factors. The drown lines show the SM prediction. In (a), the black circle with error bar denotes our result, and the neibouring white circle with large error(arrows) shows that LEP has no sensitivity for model-independent determination of $\bar{\alpha}(q^2)$.

cross section at low energies. Therefore the errors of the measurements cause the ambiguity of $\bar{\alpha}$ theoretical prediction, and numerically it is 0.1%.

This is far from no running case by $3.0\sigma$ (Fig.15), and it is the first observation of the significant running SU(2)×U(1) coupling. In the Standard Model, the running of $\bar{g}_z^2$ and $\bar{s}^2$ is small, and the measurements by the low energy and LEP experiments are consistent with the Standard Model prediction. Considering their errors, the running of $\bar{g}_z^2$ and $\bar{s}^2$ is not significant(See Fig.15(b) and (c)).

### 6.1.1 Limit to the new physics in the gauge boson sector

Our obtained $\bar{\alpha}(q^2)$ is able to give a limit to the new physics which is expressed by 6-dimensional operators of electroweak bosonic sector. These operators can cause anoumarous triple gauge boson coupling. According to the Eq.11, the obtained value of $\bar{\alpha}(57.77^2 GeV^2)$ gives a limit of $f_{DW}$ and $f_{DB}$. We obtained;

$$f_{DW} + f_{DB} = -11.4^{+12.1}_{-10.9}(\text{stat})^{+35.8}_{-34.52}(\text{sys}) \tag{25}$$

K.Hagiwara and S.Ishihara have done the global fit with this model using all available low energy experiments and 1992 LEP data[37]. Their fit results and our limit are displayed in Fig.16. This shows that we can obtain some information about the triple gauge boson coupling.

## 6.2 The determination of $\gamma - Z$ interference

Combining our result with the published data of OPAL[38], we performed a model-independent fit according to Eq.13 regarding $\bar{M}_Z$, $\bar{\Gamma}_Z$, $R$ and $J_{had}$ as free parameters using the following assumptions. The energy-dependent difference of $J_{had}$ at LEP and TRISTAN is negligible in the fit, since it is expected to be small[10] (~0.6% in the SM), and the QCD corrections are given by the $O(\alpha_s^3)$ equation in Ref.[36]. The $\chi^2$ we minimized was the sum of the $\chi^2$'s for the TOPAZ and the OPAL data:

$$\chi^2 = \chi^2_{TOPAZ} + \chi^2_{OPAL}. \tag{26}$$

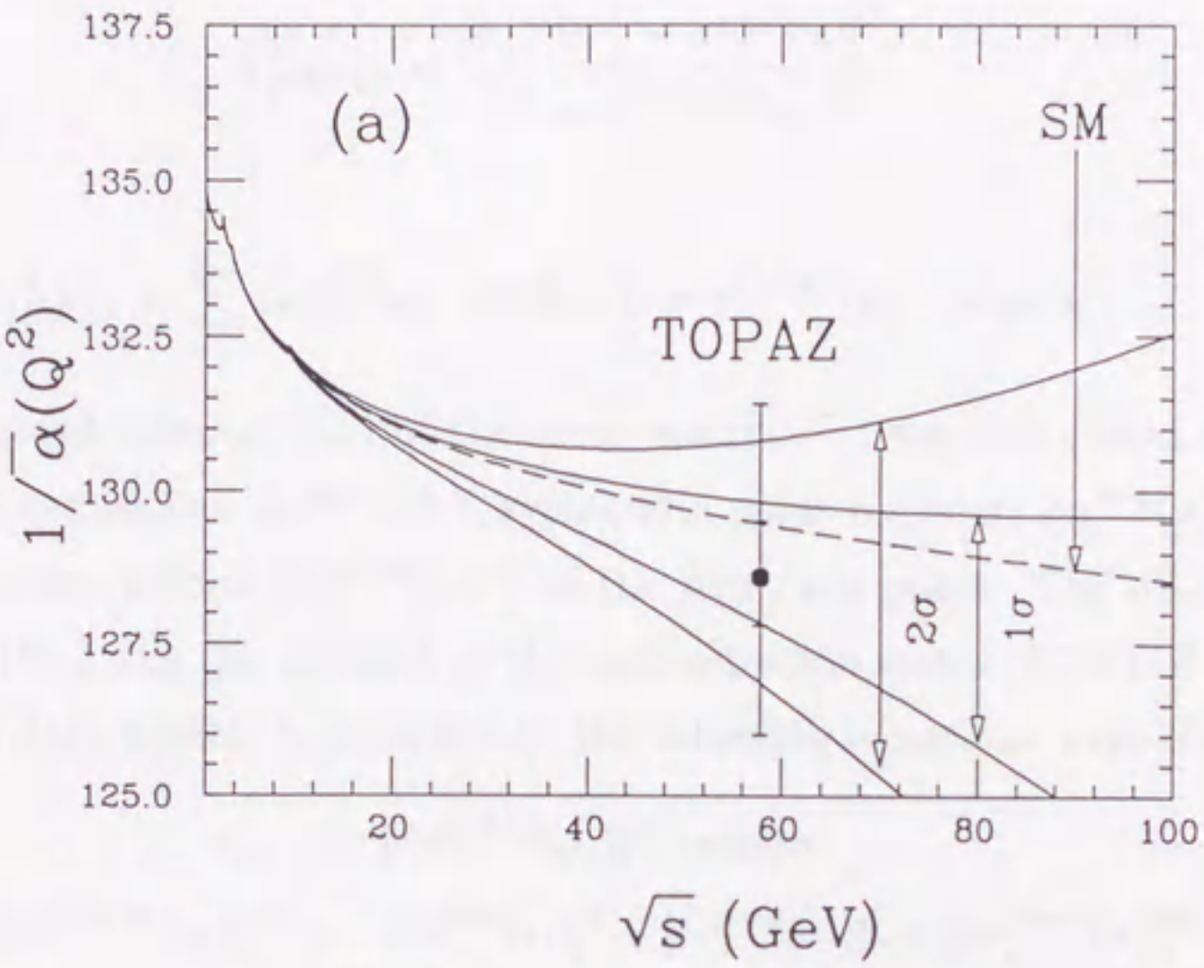


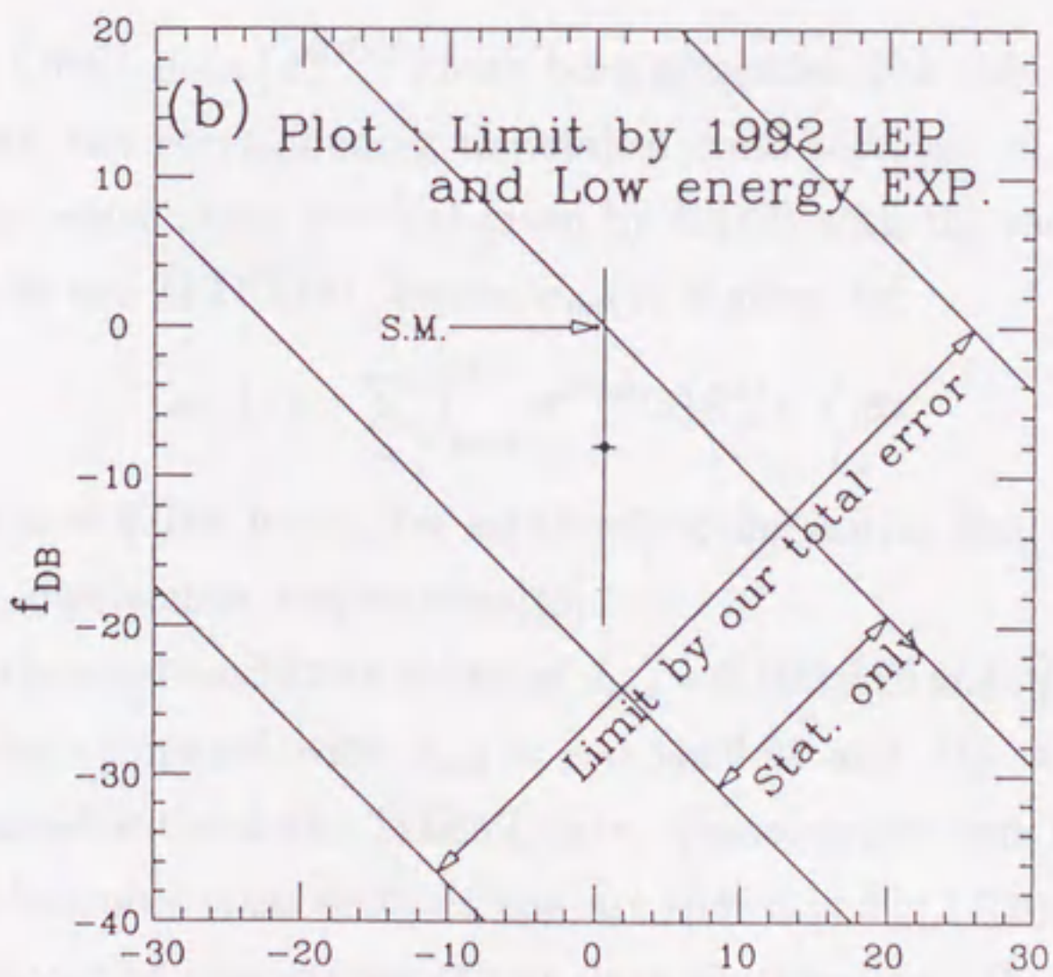


Figure 16: The operators $f_{DW}$ and $f_{DB}$ affect to the $\bar{\alpha}(q^2)$(a). Our data point put a limit on the sum of these two(b).

where $\chi^2_{TOPAZ}$ and $\chi^2_{OPAL}$ were given by

$$\chi^2_{TOPAZ} = \frac{[\sigma_h^{TOPAZ} - \sigma^{smat}(s)]^2}{(\delta\sigma_{stat})^2 + (\delta\sigma_{sys})^2} \tag{27}$$

and

$$\chi^2_{OPAL} = \sum_{i,j} \Delta_i V_{ij}^{-1} \Delta_j \quad \text{with} \quad \Delta_i = \sigma_i^{OPAL}(s_i) - \sigma_{tot}(s_i). \tag{28}$$

The diagonal element ($V_{ii}$) of the error matrix ($V$) was calculated by summing the statistical( $\delta\sigma_i^{stat}(s_i)$ ), systematic point-to-point( $\delta\sigma_i^{p-p}(s_i)$ ), and normalization errors( $\delta\sigma_i^{norm}(s_i)$ ) of the $i$-th data point. The off-diagonal element ($V_{ij}$) was the product of the normalization errors (0.7%) of the $i$-th and $j$-th data points. Consequently, the following equations were obtained:

$$\begin{aligned} V_{ii} &= [\delta\sigma_i^{OPAL}(s_i)]^2 \quad \text{where} \\ [\delta\sigma_i^{OPAL}(s_i)]^2 &= [\delta\sigma_i^{stat}(s_i)]^2 + [\delta\sigma_i^{p-p}(s_i)]^2 + [\delta\sigma_i^{norm}(s_i)]^2 \end{aligned} \tag{29}$$

and

$$V_{ij} = \delta\sigma_i^{norm}(s_i) \times \delta\sigma_j^{norm}(s_j) \tag{30}$$

Since the OPAL data ($\sigma_i^{OPAL}$) have been presented with only the acceptance corrections, the corresponding theoretical cross sections ($\sigma_{tot}(s)$) were calculated by convoluting $\sigma^{smat}(s)$ given by Eq.(3) with the radiator function provided by the ZFITTER. Hence, $\sigma_{tot}(s)$ is given by:

$$\sigma_{tot}(s) = \sum_a \int_{smin}^{s} \sigma^{smat}(s) R^a(s, s') ds' \tag{31}$$

where $smin = 0.01s$, $a$=ini, fin, ini+fin denoting initial, final state radiation and their interference, respectively[15].

From the combined fit we obtained $J_{had} = 0.10 \pm 0.26$ and $\bar{M}_Z = 91.151 \pm 0.008$ GeV, to be compared with $J_{had} = -0.34 \pm 0.98$ and $\bar{M}_Z = 91.157 \pm 0.016$ GeV obtained without the TOPAZ data. These results were translated into the total hadronic cross sections and are shown in Fig.17(b), which clearly demonstrates the importance of our data contribution. Our data point is at $\sqrt{s}$=57.77GeV with the error bar representing the statistical and systematic errors summed in quadrature. The solid line is the SM prediction. The dot-dashed lines in (b), represent the constraint from the combined fit.

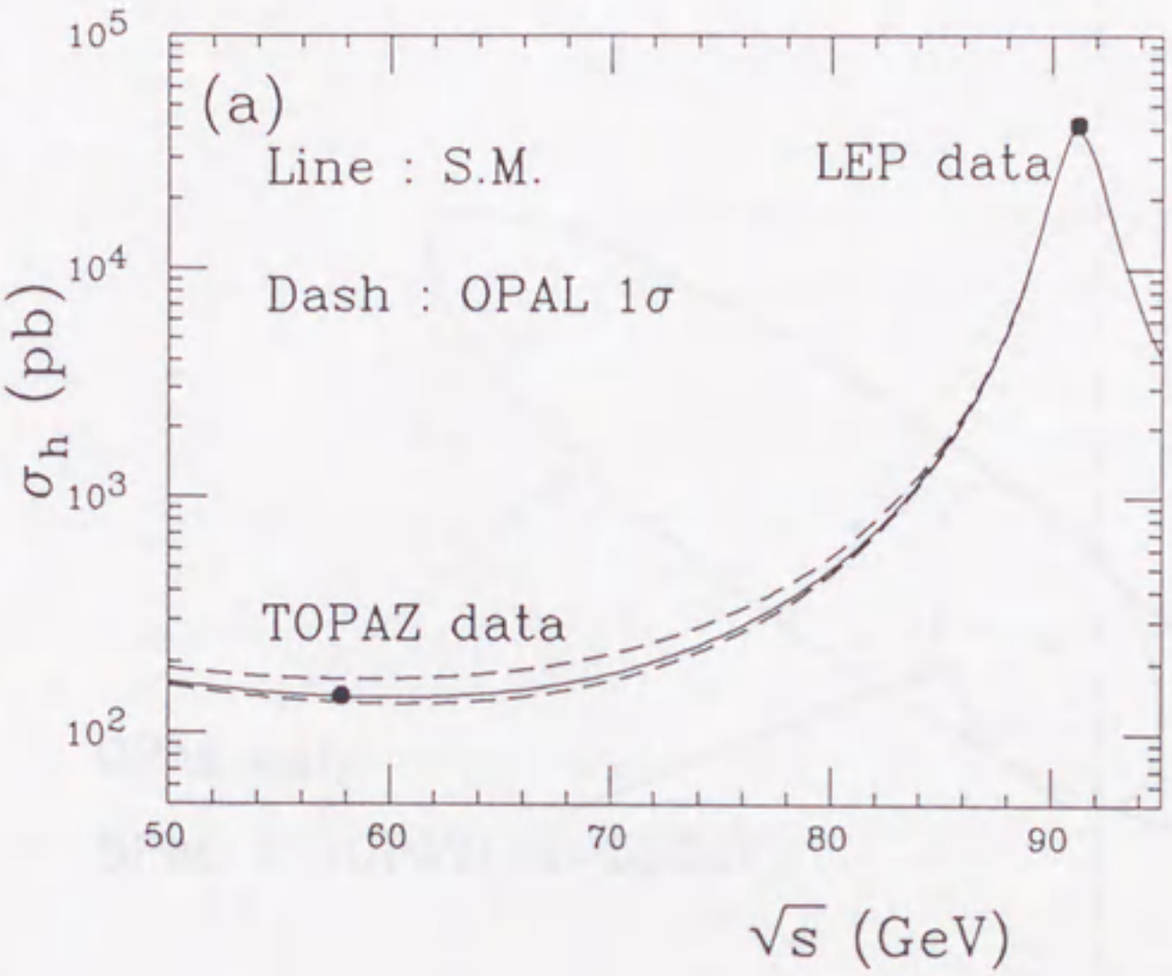


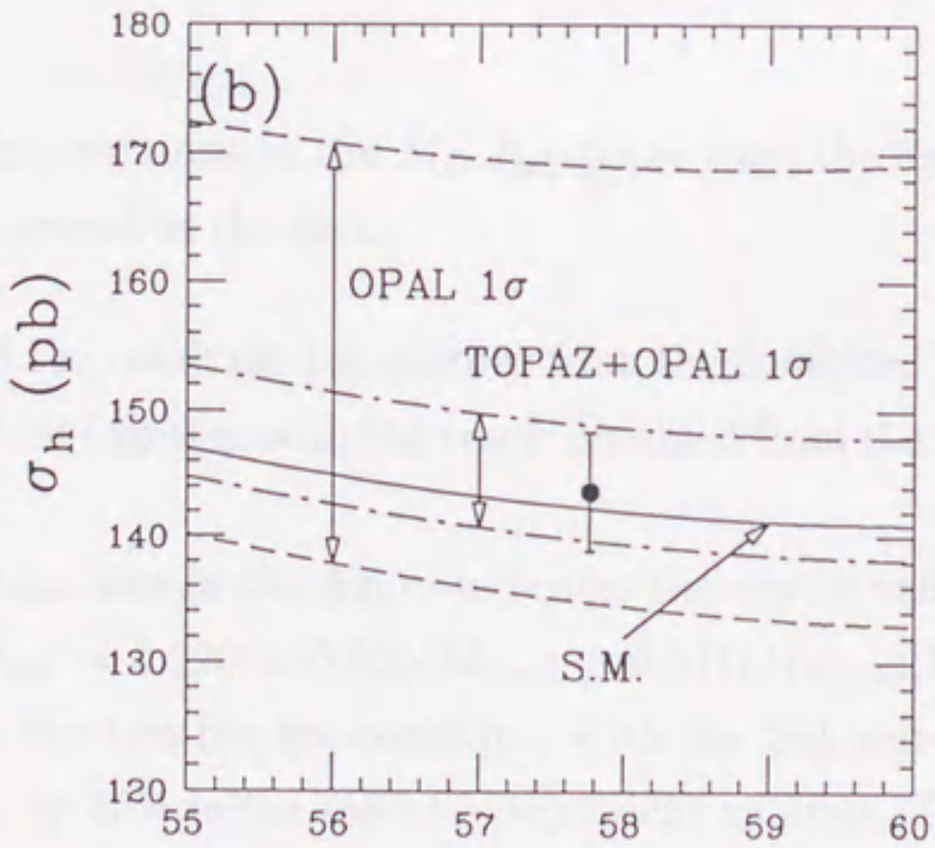


Figure 17: The $J_{had}$ effect to $\sigma_h$: (a) with both the TOPAZ and the LEP-combined[13] data plotted in the same figure, while (b) with the TRISTAN energy region magnified.

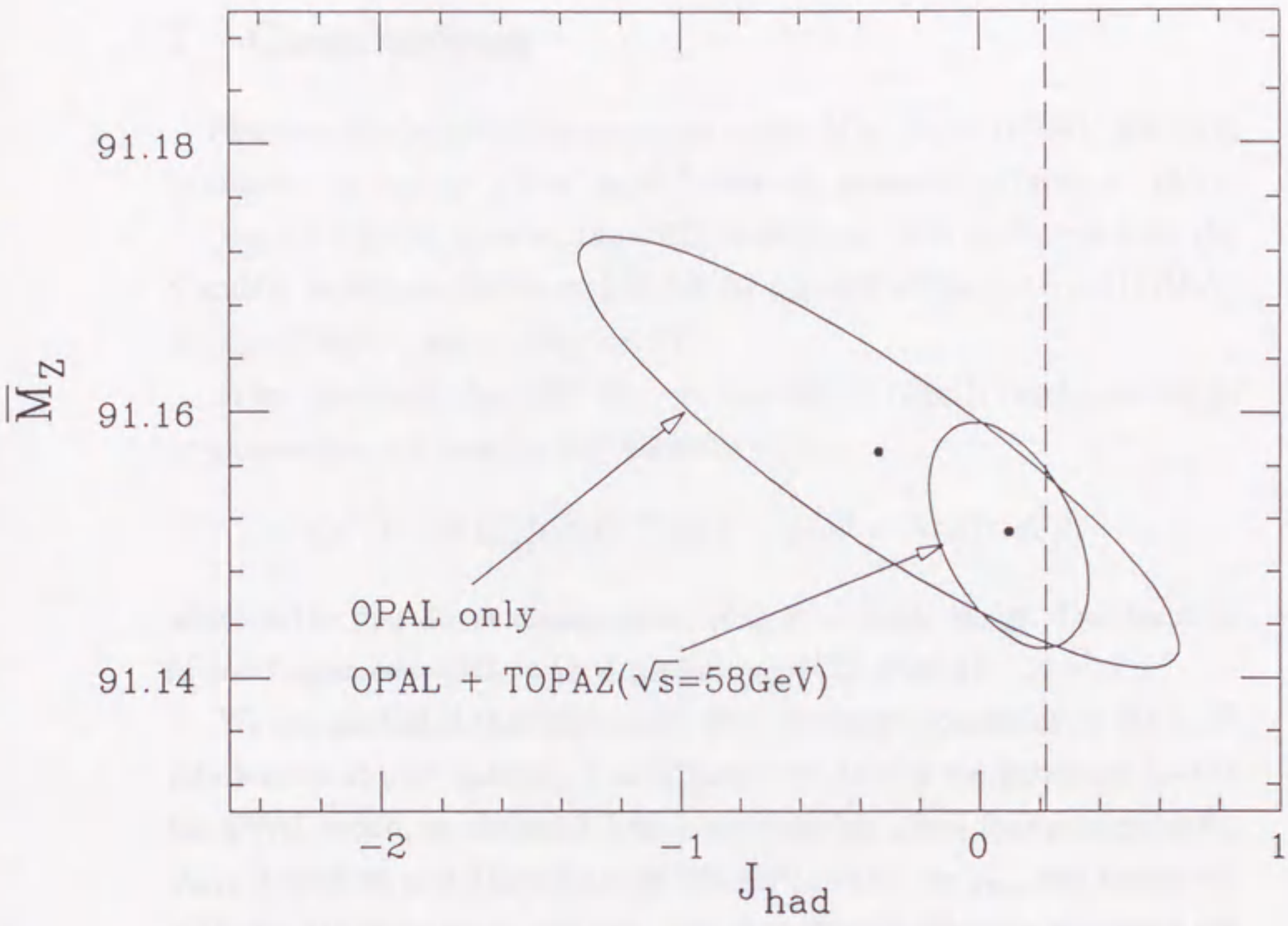


Figure 18: 1-$\sigma$ contours in the $\bar{M}_Z$-$J_{had}$ plane from the four parameter lineshape fit described in the text.

In Fig.18 the resultant 1-$\sigma$ contour from the combined fit in the $\bar{M}_Z$-$J_{had}$ plane is plotted together with the result obtained from the OPAL data alone.

The vertical line in the figure indicates the center value of the SM prediction of $J_{had} = 0.220 \pm 0.035(M_{Top}) \pm 0.011(M_{Higgs})$[16]. Although the results from the two fits are consistent with the SM, our data reduced the error on $\bar{M}_Z$ by 50% in the model-independent analysis. The resultant error on $M_Z$ is now comparable with that assuming the SM (see Fig.18).

# 7 Conclusions

Based on 9146 multi-hadronic events collected at $\sqrt{s}$=57.77GeV, the total hadronic cross section in $e^+e^-$ annihilation was measured to be $\sigma_h = 143.6 \pm 1.5(\text{stat}) \pm 4.5(\text{sys})$ pb after the QED corrections. It is consistent with the Standard Model prediction of 142.2pb for $M_Z$=91.187GeV, $M_{Top}$=174GeV, $M_{Higgs}$=100GeV, and $\alpha_s(M_Z{}^2)$=0.12.

From this result the QED effective form factor ($\bar{\alpha}(q^2)$) corresponding to $\gamma\gamma$ propagator [10] was directly obtained to be

$$1/\bar{\alpha}(q^2) = 128.6^{+0.9}_{-0.8}(\text{stat})^{+2.7}_{-2.5}(\text{sys}) \quad \text{at} \quad \text{q}^2 = (57.77\text{GeV})^2,$$

which is the first direct measurement of $\bar{\alpha}(q^2)$ at high energy. Our result is in good agreement with the SM prediction of 129.47±0.10.

We demonstrated that our results put a stringent constraint on the $\gamma$-$Z^0$ interference at LEP energies. Combing this result with the published data of the OPAL group, we obtained, from a model-independent four-parameter fit, $J_{had}$=0.10±0.26 and $\bar{M}_Z$=91.151±0.008 GeV, where the $J_{had}$ was consistent with the SM value of $J_{had}$=0.220. Our data thus significantly improved the error on $\bar{M}_Z$ in the model-independent analysis and made it comparable with that assuming the Standard Model.

## Acknowledgment

This thesis stands upon the vigorous and careful works of a great many people. This analysis was the window to see the miracle of the Universe for me, therefore it was very exciting. I would like to express my great gratitude to Prof. Ryoichi Kajikawa, Prof. Shiro Suzuki and Dr. Akira Sugiyama, who gave me a chance to take part in the TOPAZ collaboration at TRISTAN, for continuous encouragement and warm guidance. I wish to express my gratitude all members of High Energy Physics Laboratory of Nagoya University for their help and discussions.

I acknowledge all the members of the TOPAZ experiment for their supports and encouragements, and the KEK accelerator group for the excellent operation of the TRISTAN storage ring. Especially, I would like to thank Dr. Junpei Fujimoto who advised me about radiative corrections and at the same time cheered me. I would like to thank Dr. Toshiaki Tauchi, Dr. Keisuke Fujii, Dr. Akiya Miyamoto, Dr. Ichirou Adachi for their helpful discussions and cooperation.

I would like to express my appreciation to the staffs at Nara Women's University, Prof. Seishi Noguchi and Dr. Hisaki Hayashii and many motivated scientists. Particularly, in their discussions about luminosity measurement.

I am grateful to Dr. Kaoru Hagiwara and Dr. Seiji Matsumoto for their many help in discussions about electroweak radiative corrections. I also thank Dr. Tatsuo Kawamoto and Dr. Toshinori Mori for fruitful discussions about the determination of $Z^0$ parameters at LEP.

Finally I would like to thank my parents and brother for their support and warm understanding for my research life. Without their help, this thesis could not be completed.

# References


[1] S.L.Glashow, *Nucl. Phys.* **B22**, (1961) 579 .: A.Salam,in Elementary Particle Theory: Relativistic Groups and Analyticity (Nobel Symposium No.8), edited by N.Svartholm (Almqvist and Wiksell,Stockholm,1968), p361; S.Weinberg, *Phys. Rev. Lett.* **19**, (1967) 1264 .

[2] M.Kobayashi and T.Maskawa, *Prog. Theor. Phys.* **49**, (1973) 652

[3] Z physics at LEP 1 CERN-89-08.

[4] B.W.Lynn, M.E.Peskin and R.G.Stuart, in Physics at LEP, CERN86-02(1986), vol.1, p90.

[5] G.Altarelli and R.Bardieri, *Phys. Lett.* **253B**, (1991) 161 ; G.Altarelli ,R.Bardieri and S.Jadach, *Nucl. Phys.* **B369**, (1992) 3 .

[6] I.Adachi *et al.*, *Phys. Lett.* **234B**, (1990) 525 .

[7] J.Fujimoto and Y.Shimizu, *Mod. Phys. Lett.* **3A**, (1988) 581 .

[8] D.Yu.Bardin *et al.*, *Comp. Phys. Comm.* **59**, (1990) 303 .

[9] W.F.L.Hollik *DESY* **88-188**.

[10] K.Hagiwara *et al.* , "A Novel Approach to Confront Electroweak Data and Theory", KEK-preprint 93-159, April 1994, where $1/\bar{\alpha}(M_Z^2)$=128.5 assuming $\alpha_s(M_Z^2)$=0.12, $\delta_{had}$=0.0, and $M_{Top}$=174GeV.

[11] B.Griinstein and M.B.Wise, *Phys. Lett.* **265B**, (1991) 326 .

[12] M.E.Peskin and T.Takeuchi, *Phys. Rev. Lett.* **65**, (1990) 964 ; *Phys. Rev. D* **46**, (1992) 381 .

[13] CERN-PPE/93-157.

[14] S.kirsh and T.Riemann, DESY-94-125; T.Riemann, *Phys. Lett.* **293B**, (1992) 451 .

[15] D.Bardin *et al.* , CERN-TH.6443/92.

[16] G.Isidori, *Phys. Lett.* **314B**, (1993) 139 ; Martin Grünewald and Stefan Kirsh, CERN-PPE/93-188; T.Kawamoto, Private communication.

[17] D.Bardin *et al.Phys. Lett.* **206B**, (1988) 539 .

[18] H.Fukuma, KEK Proceedings 93-2,p296.

[19] I.Levine, KEK Proceedings 93-2,p282.

[20] T.Kamae *et al.* , *Nucl. Instr. Meth.* **A252**, (1986) 423 ; A.Shirahashi *et al.* , IEEE Trans. Nucl. Sci. NS-35(1988)414.

[21] H.Hayashii *et al.* , *Nucl. Instr. Meth.* **A316**, (1992) 202

[22] A.Yamamoto *et al.* , *Jpn. J. Appl. Phys. Lett.* **25**, (1986) L440

[23] S.Jadach, B.F.L.Ward and Z.Was, *Comp. Phys. Comm.* **66**, (1991) 276 .

[24] T.Sjostrand and M.Bengtsson, *Comp. Phys. Comm.* **43**, (1987) 533 .

[25] S.Jadach and B.F.L.Ward, *Comp. Phys. Comm.* **56**, (1990) 351 .

[26] D.R.Yunnie, S.C.Frautschi and H.Suura, *Ann. Phys. (NY)* **13**, (1961) 379 .

[27] G.altarelli and G.Prisi, *Nucl. Phys.* **B126**, (1977) 298 .

[28] W.Nilson et.al., SLAC-Report-265(1985).

[29] E.Longo and L.Luminari, *Nucl. Instr. Meth.* **A239**, (1985) 506

[30] H.Feaefeldt, PITHA 85/02(1985).

[31] B.Howell *et al.Phys. Lett.* **291B**. (1992) 206 .

[32] K.Muramatsu *et al.Phys. Lett.* **332B**. (1994) 477 .

[33] H.Hayashii *et al.Phys. Lett.* **314B**. (1993) 149 .

[34] S.Kuroda *et al.Comp. Phys. Comm.* **48**. (1988) 335 .

[35] R.Itoh, Doctoral thesis, University of Tokyo(1988) (unpublished)

[36] L.R. Surguladze and M.A.Samuel, *Phys. Rev. Lett.* **A66**, (1991) 560 .
S.G.Goisny, A.L.Kataev and S.A.Larin, *Phys. Lett.* **259B**, (1991) 144 .

[37] H.Hagiwara *et al.Phys. Rev. D* **48**, (1993) 2182 .

[38] OPAL coll., *Z. Phys.* **58C**, (1993) 539 .